On the control of subantarctic stratification by the ocean circulation

R. Justin Small[1] · Alice K. DuVivier[1] · Daniel B. Whitt[1] · Matthew C. Long[1] · Ian Grooms[2] · William G. Large[1]

Abstract

A shallow mixed layer depth bias in Austral winter in the Subantarctic Zone is a common feature of Coupled Model Intercomparison Project (CMIP5) models, including the Community Earth System Model (CESM). The bias is related to other deficiencies in the model solution, including too-weak Subantarctic Mode water formation and excessive leakage of Agulhas waters into the Atlantic instead of into the Indian Ocean and Subantarctic Frontal Zone. This work investigates the hypothesis that the shallow bias is due to errors in the simulated ocean circulation. Results from a model with low resolution ocean component (1° grid) are compared against: (i) an experiment with an eddy resolving (0.1°) grid and (ii) experiments using the 1° grid and employing an adiabatic nudging of the ocean pressure field to observations that is referred to as a semi-prognostic method. For both the higher resolution and semi-prognostic experiments, improved horizontal advection of warm and salty water near the surface leads to a more realistic sea surface temperature (SST) and salinity front associated with the Agulhas Return Current and Antarctic Circumpolar Current. The warmer surface waters in the high-resolution model and semi-prognostic model lead to stronger air–sea heat loss, with a response of about 40 Wm^{-2} °C^{-1} in winter in the area of deep mixed layers. Budgets of the temperature and salinity stratification show that the deeper mixed layers in the high-resolution experiment are primarily a result of the increased surface heat loss, whereas in the semi-prognostic case salinity advection is the main factor leading to destabilization of the water column. Both results indicate that ocean circulation is a key factor in wintertime deep Southern Ocean mixing, associated with advection of water masses and air–sea feedbacks.

1 Introduction

1.1 Background

The Southern Ocean is an important region for air–sea exchange of heat and anthropogenic greenhouse gases (Sabine et al. 2004; Rodgers et al. 2014; Frölicher et al. 2015) due to a combination of strong winds and temperature gradients in the ocean and atmosphere. The Southern Ocean is dominated by the Antarctic Circumpolar Current (ACC); immediately north of the ACC, large air–sea heat fluxes drive Subantarctic Mode Water formation (McCartney 1982; Hanawa and Talley 2001; Dong et al. 2008; Wang et al. 2014; Cerovečki et al. 2013). This region is characterized by an observed Deep Mixing Band (DMB: following DuVivier et al. 2018), with winter mixed layer depths (MLD) deeper than 200 m. The DMB spirals from the South-western Indian Ocean at around 40° S to Drake Passage at around 60° S and in some regions the MLD exceeds 400 m depth in the Austral winter average (Fig. 1a, b) and 500 m in individual months (Dong et al. 2008; Holte et al. 2017; DuVivier et al. 2018).
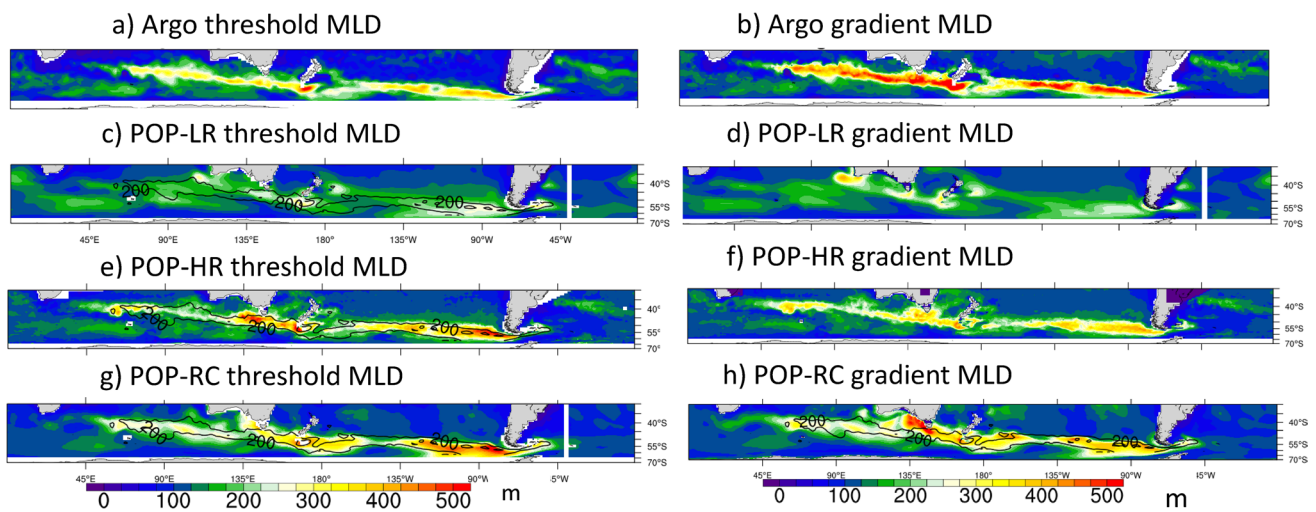
CMIP class climate models have difficulty in simulating important aspects of the Southern Ocean climate. In particular, the simulated Southern Ocean DMB has year-round shallow biases, but notably in winter these shallow biases exceed hundreds of meters (Weijer et al. 2012; Sallée et al. 2013; Meijers 2014). Additionally, the DMB occurs over a broader latitudinal extent in models than in observations (Sallée et al. 2013): an example from a climate model is shown in Fig. 1c, d. Other biases of CMIP5 models in this region include deficient mode water formation (Weijer et al. 2012); a surface fresh bias (Sallée et al. 2013); sub-surface

✉ R. Justin Small
   jsmall@ucar.edu

1 Climate and Global Dynamics Division, National Center for Atmospheric Research, 1850 Table Mesa Drive, Boulder, CO 80305, USA

2 Department of Applied Mathematics, University of Colorado, Boulder, USA

a) Argo threshold MLD

b) Argo gradient MLD

c) POP-LR threshold MLD

d) POP-LR gradient MLD

e) POP-HR threshold MLD

f) POP-HR gradient MLD

g) POP-RC threshold MLD

h) POP-RC gradient MLD

Fig. 1 Mixed Layer Depth in Argo and forced ocean models in Austral winter, JAS. **a**, **b** From ARGO float observations, **c**, **d** low resolution ocean model POP-LR, **e**, **f** high resolution ocean model POP-HR, **g**, **h** low resolution ocean model with semi-prognostic method applied in whole Southern Ocean, POP-RC. The left hand panels use a density threshold of 0.03 kg m^{-3} to determine MLD. For the right panels, the gradient method of Large et al. (1997) is used. The 200 m and 400 m MLD contours from **a** are overlaid on **c**, **e**, **g**, **h**. **a**–**f** Are averages of years, 2005–2009, while **g**, **h** is for the CORE normal year (Large and Yeager 2004)

salinity biases (DuVivier et al. 2018); insufficient air–sea heat loss (Lee et al. 2011); and too much leakage of Agulhas system waters into the Atlantic (Weijer et al. 2012). In this paper we show that many of these biases are interlinked and all affect the climatological MLD in the DMB: hence the MLD is difficult to simulate in climate models. Then, in turn, these physical biases may be connected with biases in CFC and CO_2 uptake (Doney et al. 2004; Long et al. 2013).

Many approaches have been applied to improve the DMB biases in the CMIP class models. These include efforts to better understand and represent vertical mixing by wind-driven near-inertial waves (e.g., Jochum et al. 2013; Forryan et al. 2015), by wind-forced submesoscales (e.g., Thomas 2005; Whitt and Taylor 2017; Bachman et al. 2017), and by wave-driven Langmuir turbulence (McWilliams et al. 1997; Van Roekel et al. 2012; McWilliams et al. 2014; Li and Fox-Kemper 2017; Reichl et al. 2016; Large et al. 2019). An approach that appears to improve some aspects of the depth and spatial distribution of the DMB is to use climate models with an eddy-permitting (Lee et al. 2011) or eddy-resolving (McClean et al. 2011; Li and Lee 2017) ocean model. Previous work has also established that some aspects of the deep mixed layers and associated mode waters of the Subantarctic Ocean are sensitive to the ocean circulation (e.g. Herraiz-Borreguero and Rintoul 2011; Li and Lee 2017; DuVivier et al. 2018). The present investigation follows this latter aspect, and links the above-stated physical biases to the ocean general circulation.

We believe that the current study is the first to quantify the role of two key processes by which the circulation effects the stratification and DMB: i) oceanic heat transport from low-latitudes and consequent air–sea heat loss over the warm side of the Subantarctic Front, and ii) salinity transport from low latitudes into the Subantarctic zone (building on the regional studies of Wang et al. 2014 and Lee et al. 2011). The paper conducts a circumglobal study of these processes via experiments with both low and high resolution and by using a modified pressure field at the low resolution (and thus a modified geostrophic flow) that matches observations (using the method of Greatbach 2004). Our intent is not to explain the dynamics of the circulation, instead the focus is on how changes in circulation effect the stratification, using the model experiments and with reference to observations. The results show that biases in the simulated geostrophic current are a dominant cause of the biases in the thermohaline transport, the resulting air–sea flux feedback, and hence the order-one biases in the wintertime mixed layer depth and surface heat flux in the CMIP-class ocean/sea-ice model.

However, this work is just one step toward fully elucidating the impact of ocean circulation on the Subantarctic stratification and the causes of the associated biases there; it complements other efforts to quantify the impacts on DMB simulation of various unresolved small-scale upper-ocean processes (described above), variations in the atmospheric or sea-ice forcing (e.g., Gao et al. 2018; Cerovecki et al. 2019), salinity profiles in the main thermocline (e.g., DuVivier et al. 2018), or atmospheric biases in fully-coupled atmosphere–ocean models (e.g., Hyder et al. 2018).

The paper is organized as follows: Sect. 2 describes model systems and experiments, observational benchmarking datasets, and model heat and salinity budget approaches. The observed and modelled Southern Ocean MLD, air–sea heat

flux, and temperature and salinity characteristics, including their relative roles in governing density stratification in Austral winter are compared in Sect. 3. The longitudinal structure of the region of deep mixed layers is discussed in detail in Sect. 4, including local centers of action and downstream propagation. Section 5 then presents heat and salinity stratification budgets from models to explain differences in stratification between the models and observations. (Note that short summaries are provided at the start of each results section.) This is followed by a Discussion of further implications of the results (Sect. 6), and then Conclusions.

2 Models, data and methods

2.1 Ocean-Sea ice simulations

The current study uses ocean models with identical vertical mixing physics and forced by the same atmospheric state, but with very different ocean circulation. The ocean model is coupled to a sea-ice model, and is forced by an atmosphere-state dataset configured to be appropriate for forcing ocean models. Fully coupled models are not focused on here because of the large atmosphere-state biases in the S. Ocean in most CMIP class models, including too-strong wind stress, as well as cloud, temperature and humidity errors (Hyder et al. 2018).

All presented ice-ocean experiments (Table 1) use the Parallel Ocean Program version 2 (POP2, Smith et al. 2010; Danabasoglu et al. 2012) and Los Alamos Sea Ice Model, CICE version 4 (Hunke and Lipscomb 2008) run in the framework of the Community Earth System Model version 1 (CESM1, Hurrell et al. 2013). In each experiment CICE and POP share the same grid. The surface forcing is either CORE Interannual Forcing (Large and Yeager 2009) or CORE Normal Year forcing (Large and Yeager 2004) as specified in Table 1. The coupler computes air–sea fluxes using the ocean sea surface temperature (SST) and surface current as described by Large and Yeager (2009).

The POP-Low Resolution (POP-LR) configuration has nominal 1° spacing, in a dipole grid with the northern pole displaced to over Greenland, with 62 vertical levels. POP-LR uses the following parameterizations: ocean mesoscale processes represented by the Gent and McWilliams parametrization (Gent and McWilliams 1990) as modified by Danabasoglu et al. (1995); vertical mixing physics by the K Profile parametrization (KPP: Large et al. 1994); submesoscale mixed-layer processes by the Fox-Kemper et al (2011) parametrization; and dense overflows as in Danabasoglu et al. (2012).

The companion simulation POP-High Resolution (POP-HR) has nominal 0.1° spacing (decreasing from about 11 km at the Equator to 2.5 km at high latitudes) in a tripole grid

with poles in North America and Asia and 62 vertical levels. POP-HR uses the same KPP physics as POP-LR, but because of the higher resolution does not include any mesoscale or overflow parameterizations, nor does it include sub-mesoscale parameterization.

2.2 Semi-prognostic method for currents in low resolution model

The Greatbatch et al. (2004) semi-prognostic method is an adiabatic nudging of the ocean pressure field to observations. It is known as an adiabatic method, as it does not introduce extra source terms in the temperature and salinity equations. Instead, temperature and salinity are improved via changes in advection resulting from the altered flow field. In our experiments this method is used in the 1° configuration and results in a more realistic flow field for this configuration. The application of the semi-prognostic technique in this work was motivated by the fact that it has been used previously to improve circulation in a limited region and investigate the downstream effects, such as in the Gulf Stream/North-west corner region (Sheng et al. 2001; Greatbatch et al. 2004; Weese and Bryan 2006; Drews and Greatbatch 2017). Thus it is a method of interest in the Southern Ocean, where the ACC and Subantarctic zone is expected to be influenced by influxes of heat and salt from boundary systems such as the Agulhas Return Current (ARC) and East Australian Current.

The semi-prognostic method is applied as follows. Within a specific geographic region[1] the density field used in the model hydrostatic equation is fully replaced[2] with an observed density field (from World Ocean Atlas 1998, Levitus et al. 1998[3]), a monthly climatology. The mean geostrophic flow field is thus mainly determined from this correction. POP-Realistic Current (POP-RC) uses the semi-prognostic method throughout much of the Southern Ocean and Equatorward, namely in the circumglobal region of 25° S to 65° S, with a transition zone of about 5° width at either edge over which the model density replacement decays from full to zero.

A companion control simulation, with exactly the same model version, forcing, and initialization but without the semi-prognostic method was also performed, referred to as POP-LR-EXT (Table 1a). As with POP-RC, this simulation also output the variables necessary to compute heat and

---

[1] However nudging is not applied within two grid points of bathymetry/coastline to ensure stability of the solution.

[2] Thus, strictly we are using a mostly diagnostic approach, rather than semi-prognostic, but we refer to it as semi-prognostic because of the familiarity of the term in the literature.

[3] Although more-up-to-date databases are available, we found that WOA98 was sufficient to demonstrate the main results of this paper.

Table 1 List of Ocean-ice Experiments

Name	Ocean Grid Spacing	Notes
a) Main experiments		
POP-LR	Nominal 1°	POP forced by CORE Interannual Dataset (Large and Yeager 2009; Danabasoglu et al. 2012) Run starts at year 1948: years 2005–2009 analyzed
POP-HR	Nominal 0.1°	POP forced by CORE Interannual Dataset (Johnson et al. 2016) The run started at year 1977;years 2005–2009 analyzed. Control experiment for comparison is POP-LR
POP-RC	Nominal 1°	Semi-Prognostic restoring of currents done in region of 25° S to 65° S Transition zone of about 5° width. POP forced by CORE Normal Year[a] Dataset. Initialized on Jan. 1st from year 293 of a previous long control run at 1° Years 293–310 are used to compute averages except where noted otherwise Control experiment for comparison is POP-LR-EXT
POP-LR-EXT	Nominal 1°	As POP-LR, but forced by CORE-Normal Year. EXT refers to extended output variables used for heat and salinity budgets. Initialized same as POP-RC. Years 293–310 are used to compute averages

Name	Region	Refer to Fig
b) Regional semi-prognostic experiments, all at 1°		
Inclusion experiments		
Agul ellipse	Included region: Ellipse covering the south-west Indian Ocean and also large part of the S. Atlantic	8b
Agul-Australia	Included region: Similar to Agul but ellipse center is further east so that region covered is south-west Indian Ocean to longitude of New Zealand	8c
Agul-New-Zealand	Included region: Wider than Agul-Australia and now covering part of Pacific Ocean east of New Zealand and part of Atlantic	8d
Exclusion experiments		
No-Agul	Excluded region: Ellipse covering the south-west Indian Ocean and also large part of the S. Atlantic	8e
No-Agul-New-Zealand	Excluded region: Ellipse covering the south Indian Ocean and western part of Pacific and part of Atlantic	8f

A list of the experiments discussed in the text, including their grid spacing, and notes including the type of forcing, the years of experiment, initial conditions, and any other features. Table 1a contains the main experiments used for Sects. 3, 4.2 and 5, and Table 1b describes the regional semi-prognostic experiments (Sect. 4.1). All experiments are run with sea-ice model CICE4 on the same grid as POP. Note that the actual spacing of POP-LR is uniform at 1.125° in the zonal direction but varies from 0.27° in meridional direction at the equator, to around 0.5° at higher latitudes (Danabasoglu et al. 2006). The grid spacing of POP-HR in both directions is 0.1°cos(lat) where ° refers to a degree of latitude. Right column in b shows the Figure where the domain is shown. Note that for all experiments in b, the control is POP-LR-EXT

[a]The mixed layer bias in low resolution POP forced by CORE Normal Year (NY) is very close to that when forced by CORE Interannual Forcing. POP-RC has been compared to POP-LR and also against a control with CORE-NY giving almost identical results.

Fig. 2 a, **b** The seasonal cycle of Southern Ocean mixed layer depth and wind stress magnitude. **a** Austral summer, **b** Austral winter. Colors show mean wind stress magnitude The corresponding seasonal mixed layer depth is overlaid, with contours of 60 m, 80 m for JFM and 200 m, 400 m for JAS. Observations are from Argo floats gridded MLD climatology and QuikSCAT data produced by Risien and Chelton (2008). **c** Air-sea heat loss in Austral winter from Trenberth and Fasullo (2017) with mixed layer depth contoured
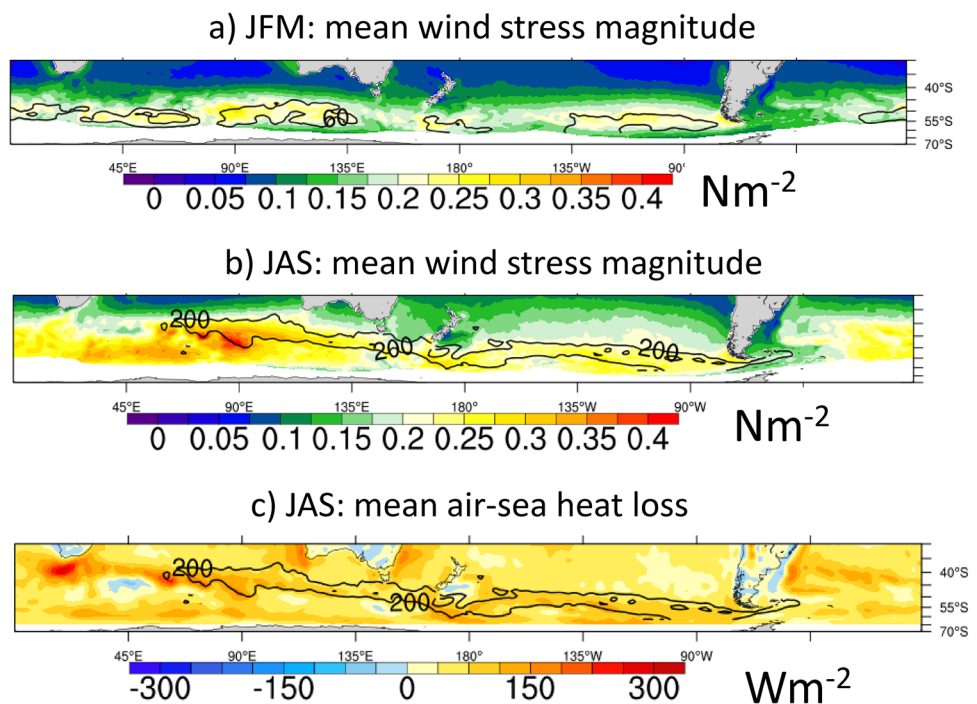
salinity budgets. The main difference between POP-LR-EXT and POP-LR is that the former uses CORE "normal-year" forcing (Large and Yeager 2004) whilst the latter uses CORE interannual forcing (Large and Yeager 2009). The important aspects of the climatology studied in Sect. 3 are almost identical in POP-LR and POP-LR-EXT, and consequently in the text of Sects. 3–5 we do not distinguish between POP-LR and POP-LR-EXT and simply use "POP-LR" to refer to these low resolution experiments. The control experiments are listed in Table 1.

The semi-prognostic method was also applied in different regions of the Southern Ocean to help identify specific regions controlling MLD distribution. Experiment names are listed in Table 1b, and the regions are defined by ellipses as illustrated in Fig. 8 below. Excepting the domain definition, these experiments were identical in set up and initial conditions to POP-RC. More details on these experiments are contained in Sect. 4.1.

2.3 Observational datasets and products

Argo floats (Argo 2019) have revolutionized knowledge of the Southern Ocean DMB (Dong et al. 2008; Roemmich et al. 2009; Holte et al. 2017), in particular its geographical distribution. We use the 1° gridded Argo data from (Roemmich and Gilson 2009) freely available at: https://sio-Argo. ucsd.edu/RG_Climatology.html. As detailed in DuVivier et al. (2018), we focus on the years 2005–2009 to correspond to available years from the POP-LR and POP-HR simulations. It is acknowledged that this period is short,

particularly as interannual variability of observed MLD is quite high (Supp. Fig. S1), and also that Argo data gave more dense coverage in more recent times (see e.g. Heuzé et al. 2015). Comparisons of the 2005–2009 period with longer records revealed that the 2005–2009 average is quite representative (Supp. Figs. 2, 3).

As the Southern Ocean meteorology has traditionally been under-sampled, several air–sea flux datasets are compared in Appendix A to establish uncertainty in the net heat flux and the Trenberth and Fasullo (2017) dataset is selected as a representative case. Trenberth and Fasullo (2017) use an indirect method to compute net surface heat loss by finding the residual between the Top of Atmosphere radiative fluxes from satellite data, and the internal atmosphere heat transports from ERA-Interim (Liu et al. 2015). This method provides only the net surface air–sea flux and cannot separate individual contributions from latent and sensible heat and shortwave and longwave radiation.

The wind stress climatology dataset prepared by Risien and Chelton (2008) from QuikSCAT scatterometer data is used. Other datasets give similar results regarding whether the spatial distribution of winter MLD is related to regions of strong wind stress.

2.4 Definitions of mixed layer depth and stratification

Two different approaches to computing MLD are used. In the first approach the MLD is obtained from monthly mean temperature and salinity profiles using the density threshold

Fig. 3 Density stratification given by potential density (PD) difference: PD(400 m)-PD(surface) from regridded Argo float data for different seasons. **a** Summer (JFM), **b** winter (JAS) and **c** Annual mean. See color bar in **c**. More positive values denote stabilizing, more negative destabilizing. Contours of MLD from Argo in JAS are overlaid at 200 m, 400 m intervals
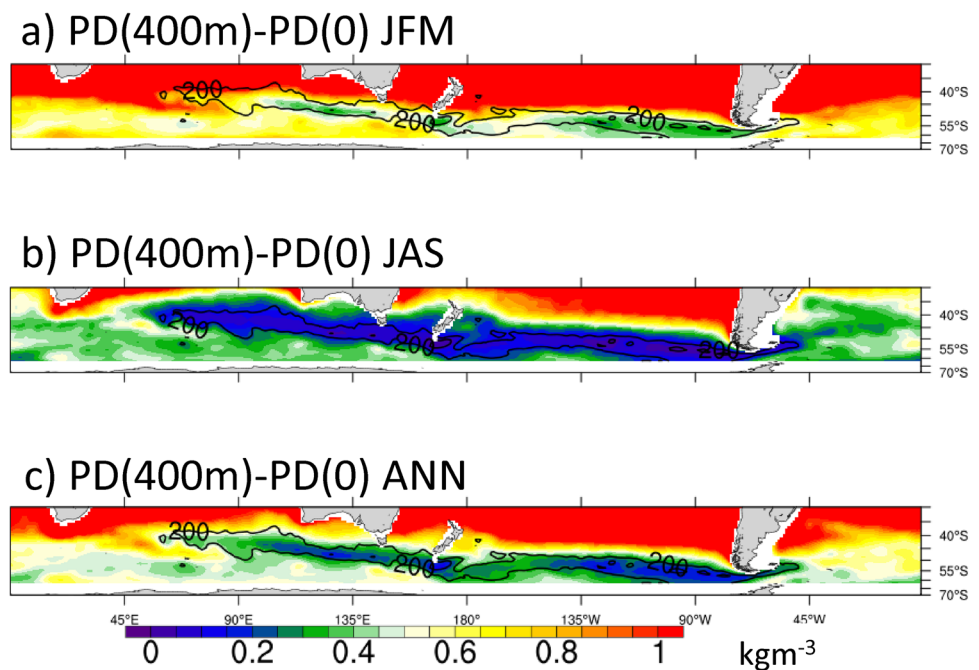
of 0.03 kg m^{-3} (e.g. de-Boyer Montégut et al. 2004). The same MLD definition is applied to model simulations. The second approach uses the Large et al. (1997) definition, which is based on identifying the buoyancy frequency maximum (see also Whitt et al. 2019), and is referred to here as the gradient method. In this latter case, the computation is done on individual profiles of Argo, and the consequent MLD values averaged in time (Whitt et al. 2019). For the model simulations, the MLD is computed using the gradient method online every timestep and averaged. The results from the two definitions of MLD are compared in Sect. 3.5.

In the text we use several measures of stratification as represented by differences between quantities at two levels. In most cases, stratification refers to the difference of the quantity (potential density (PD), potential temperature or salinity) between 400 m[4] and the surface. In addition, shallow stratification (e.g. $PD_{shallow}$) refers to the difference between 200 m and the surface, and deep stratification (e.g. PD_{deep}) to that between 400 and 200 m. Finally, for the heat

and salinity stratification budgets, a definition is used that vertically averages the difference between the quantity at a depth z and that at 400 m, as described in full below.

2.5 Heat and salinity stratification budgets and time-averaging method

The heat budget in the POP model can be written as:

$$\rho_0 c_p \frac{\partial T}{\partial t} = \rho_0 c_p \left\{ -\nabla \cdot \underline{u}T + \frac{\partial}{\partial z} \kappa \left(\frac{\partial T}{\partial z} - \Gamma \right) + P \right\}, \quad (1)$$

where T is potential temperature, ρ_0 a reference ocean density, c_p heat capacity of the ocean, ∇ is the 3D gradient operator, $\underline{u}$ the 3D velocity, κ the vertical diffusivity and $\kappa\Gamma$ the KPP non-local vertical flux of temperature, and P includes the 3D convergence of other parameterized transport, such as Gent-McWilliams (1990) and Redi (1982) parameterizations of eddy heat flux, and the Fox-Kemper et al. (2011) submesoscale parameterization. Vertically integrating to a depth H gives

$$\rho_0 c_p \int_{-H}^{0} \frac{\partial T}{\partial t} \partial z = -\rho_0 c_p \int_{-H}^{0} (\nabla \cdot uT + P)\partial z - Q - \rho_0 c_p \kappa \left(\frac{\partial T}{\partial z} - \Gamma \right)_{-H} - Q_{p-H} \quad (2)$$

$$\text{i} \qquad\qquad \text{ii} \qquad \text{iii} \qquad \text{iv} \quad \text{v} \qquad\qquad \text{vi}$$

---

[4] 400 m is chosen as it is a representative depth to which Argo, POP-HR and POP-RC can sometimes mix in the DMB, but is much deeper than the POP-LR MLD. Therefore, understanding the stratification between the surface and 400 m should offer some insight into why the MLD is so different between these cases.

where Q is the surface heat flux, with positive values denoting heat loss, Q_p the penetrative heat flux (now separated from the rest of the vertical mixing term). Here term (i) is the heat content tendency, (ii) the 3D resolved advection, in

other words the resolved flux convergence since the flow is non-divergent, (iii) the convergence of parameterized heat transport, (iv) the air–sea heat flux, term (v) is the interior mixing at depth H and (vi) the penetrative radiation. For convenience terms (ii) and (iii) will be lumped together and called the Ocean Heat Flux Convergence (OHFC). For POP-LR the above terms are saved monthly. For POP-HR all terms were saved except term P, which just includes horizontal (biharmonic) diffusion, and penetrative short-wave radiation, and the latter two are lumped together as a small residual, whilst for POP-LR the small residual is due to any errors in reconstructing the budget. The residual was checked to be much smaller than the terms on the right hand side *and* the heat content tendency, and a similar check was done for salinity below. Term (v) will be referred to as interior vertical mixing (VMIX) and term (iv) and (v) will be lumped together as VDIFF below. Note that for POP-HR the eddy heat flux is included in the resolved advection (term ii) but in the low resolution model it is included in term P.

An equivalent budget for salinity is:

$$\int_{-H}^{0} \frac{\partial S}{\partial t} \partial z = -\int_{-H}^{0} (\nabla \cdot uS + P_s)\partial z - \kappa_s \left(\frac{S}{z} - \Gamma_s\right)_{-H} + S_{ref}(E - Pr)$$

(3)

where S_{ref} is a reference salinity (34.7 psu here), E is evaporation, Pr precipitation and runoff, and subscripts s are used to distinguish from the temperature equation above.

We follow an approach motivated by Lee et al. (2011), who investigated the vertically integrated stratification relative to a depth H, i.e.

$$\int_{z=-H}^{0} (\rho(z) - \rho(-H))dz = \int_{z=-H}^{0}\int_{s=-H}^{z} \frac{\partial \rho}{\partial s}dsdz.$$

Here the equivalent double integral is shown to explain the relationship to vertical density gradient $\partial\rho/\partial s$ where s is a depth coordinate. This approach is modified here to deal with temperature and salinity separately, and is presented as vertically averaged stratification relative to depth H, T_{strat} and S_{strat}, defined as:

$$T_{strat} = \frac{\int_{z=-H}^{0} (T(z) - T(-H))dz}{H} \text{ and } S_{strat} = \frac{\int_{z=-H}^{0} (S(z) - S(-H))dz}{H}$$

(4)

Here H is a depth just below the deepest mixed layer in the annual cycle, and the quantity T_{strat} measures how much the upper ocean temperature is cooled or warmed relative to the temperature at a relatively quiescent depth H. Similarly, S_{strat} describes how the salt content at the fixed depth compares to the upper ocean average.

3 Sensitivity of ocean state to model resolution and to representation of currents

In this section we first review the seasonal cycle in the Subantarctic Zone from observations, and show that despite the large seasonal changes in wind stress, air–sea heat flux, and mixed layer depth, the stratification between depths of ~ 200 m and 400 m remains weak year-round. This is followed by an analysis of the bias of MLD and stratification in the POP-LR simulation and related biases in SST, sea surface salinity (SSS) and surface heat flux. Next, we identify the sensitivity of these quantities to improving resolution and/or the ocean circulation using the POP-HR and POP-RC experiments. The increase of surface salinity and the air–sea heat flux feedback in the DMB are important processes identified in this section.

3.1 Observational context

To a first approximation, deep MLDs in late winter in the extratropics are a manifestation of the seasonal cycle of local air–sea buoyancy flux and surface wind stress that has been extensively observed and modeled in a one-dimensional framework in the Northern Hemisphere (Large et al. 1994 and models reviewed therein). In the extratropical Southern Hemisphere, the wind stress has a large seasonal cycle (Fig. 2a, b), with larger maximum wind stress in winter, and strong winds occurring over a broader meridional extent in the winter storm track (compare Fig. 2a, b). Further, the net air–sea heat flux changes from mostly heat gain in summer (not shown) to heat loss in winter (Fig. 2c). Given this large seasonal cycle of forcing, it is expected that the MLD will be much deeper in winter, as observed (contours in Fig. 2a, b, note change in contour interval).

Looking in more detail, DuVivier et al. (2018) showed that local surface forcing could not explain the geographic distribution of the winter DMB. This can also be seen in Fig. 2, with the winter DMB occurring over a fairly narrow range of latitudes (about 5°–10°, see also DuVivier et al. 2018) despite the broadening of the storm track in winter. In addition deepest MLDs in winter do not seem to occur in the region of largest winter air–sea heat loss, which is west of 60° E in the Agulhas retroflection.

These results imply that subsurface or horizontal transport processes must also be important, in addition to surface forcing. One subsurface factor important to the amplitude of the seasonal MLD cycle and magnitude of deep winter MLD is the ocean stratification. Stratification influences the sensitivity of the MLD to air–sea fluxes (e.g., Deardorff et al. 1969; Pollard et al. 1972; Large et al. 1994; DuVivier et al.

2018) and can be influenced by the ocean circulation (e.g., Luyten et al. 1983; Vallis 2000).

Argo observations show that despite the large seasonal differences in MLD, the density stratification, (see Sect. 2.4 for the definitions of stratification used here), is weakest in the DMB region *relative to the surrounding ocean* in both Austral summer and winter (Fig. 3). This year-round weak stratification preconditions the DMB region for the deep winter MLD as follows: the weak stratification in the DMB below the seasonal mixed layer and thermocline implies that in Fall, once the seasonal layer is mixed through, there is potential for the MLD to get very deep. In fact, the deep stratification shows nearly identical patterns of very weak stratification in the DMB during the summer and winter season (Supp. Fig S4).

3.2 POP-LR stratification and surface fields in Austral winter

In POP-LR the winter MLD are typically shallow and the DMB too broad in the meridional direction (Fig. 1a–d). The negative MLD biases relative to Argo appear as a narrow band starting at 45°E extending eastward to Drake Passage and are generally co-located with the DMB (Fig. 4a). These differences, which typically reach 100–200 m for the MLD threshold method, are large compared to the actual threshold MLD in Argo (250–400 m, Fig. 1) and are statistically significant (Supp. Fig. S5a). (Note that Sect. 3.5 will discuss the differences between the two MLD definitions used in Fig. 1.) As to be expected from this result, POP-LR is too stratified in potential density between the surface and 400 m, relative to the Argo float observations, in the DMB (Fig. 4b). In fact POP-LR is too stratified in temperature between the surface and 400 m in the DMB (Fig. 4c), whilst it is too stratified in salinity in the Pacific Ocean DMB, but closer to observed values in the Indian Ocean DMB (Fig. 4d).

The contributions of temperature and salinity to differences in density stratification are quantified in Appendix B, where an Equation of State (EOS) with local expansion coefficients is applied to the model temperature and salinity stratification differences, first separately and then in combination. The over-stratification of density in the Indian Ocean in POP-LR relative to Argo observations is found to be due mainly to temperature, whilst in the Pacific Ocean it due to both temperature and salinity errors in the western basin and mainly salinity errors in the eastern basin. These findings are consistent with the sign of the model biases in Fig. 4b–d.

In addition, POP-LR has a cold and fresh surface bias in the DMB relative to Argo (Fig. 4e, f) which appears to originate south of S. Africa in the Agulhas Retroflection and extends all the way to Drake Passage. The SST and sea surface salinity (SSS) biases are generally larger in magnitude

in the Indian Ocean than the Pacific Ocean (Fig. 4e, f), and they are mostly confined to the DMB in both sectors (Fig. 4e, f) except that west of 180° longitude the fresh bias also extends northward toward the subtropics (Fig. 4f).

POP-LR also exhibits a deficit of heat loss to the atmosphere of 40–80 Wm^{-2} in the DMB region relative to observational analyses (Fig. 4g), which is large compared to full field values from the observations in JAS which are typically 60–120 Wm^{-2} in the DMB (Fig. 2c, Supp. Fig. S7c). It can also be noted that the surface heat loss bias (Fig. 4g) has a similar pattern to that of SST bias (Fig. 4e) and in the next sub-section it will be shown that this is a consequence of air–sea heat flux feedback to SST.
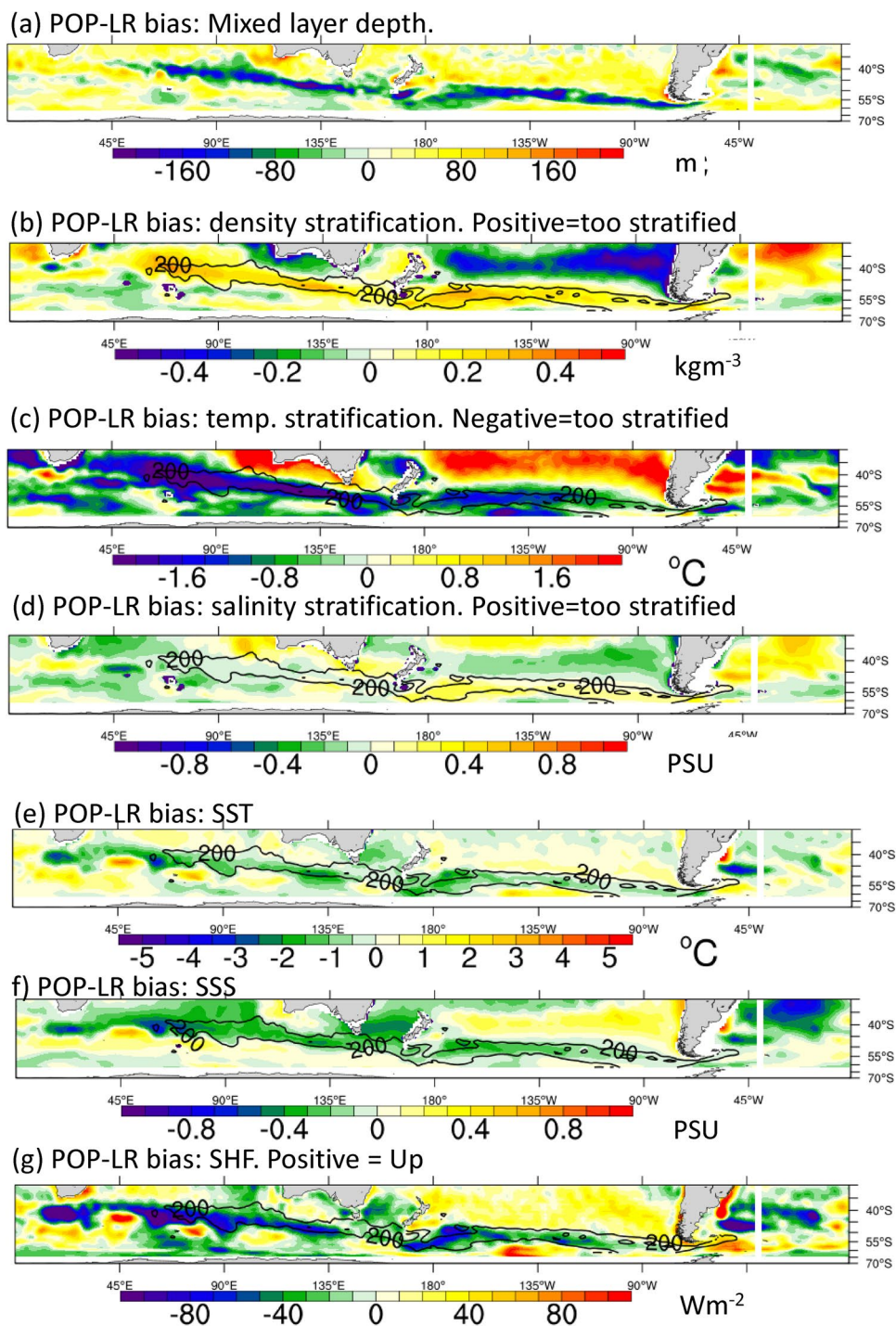
The results shown in Fig. 4 can be summarized by creating an "along-DMB section", which, for each longitude, comprises the value of a variable averaged over the latitudes where the MLD in Argo exceeds 200 m (i.e. the first contour shown in Fig. 1c etc.). (This is more instructive than using a fixed range of latitudes for each longitude due to the general poleward spiraling of the DMB.) This method shows the model biases, as seen by viewing the POP-LR minus observation results in Fig. 5 (blue lines, and statistics in Table 2). For example the shallow MLD bias is clear (Fig. 5a), as are biases in density and temperature stratification (Fig. 5c, d), and related surface quantities are shown in Fig. 6a–c). In Figs. 5, 6 uncertainty in the results is estimated by showing statistical significance at 95% following the student t-test (here the number of samples used for estimation is the 5 winter seasons for 2005–2009: see Sect. 2.3 and Supp. Figs. S2, S3 for comparison with longer periods). In addition, complementary Supp. Figs S6, S7 show the full fields from observations and model, with an indication of their spread, which is also useful to interpret the results. It can be seen that the biases in POP-LR are almost always statistically significant (Figs. 5, 6) with some exceptions including salinity stratification in the Indian Ocean (Fig. 5e) which compares quite well with observations as noted above. Section 3.4 discusses the POP-HR and POP-RC results in the same manner for comparison.

3.3 Comparison of horizontal flow between observations and model simulations

Before describing the changes to stratification in different model simulations, we first document the nature of the horizontal flow in the simulations compared to observations. (Note that vertical motion, specifically vertical advection, is addressed in Sect. 5.) Specifically we use the dynamic height between 1000 m and the surface, and its horizontal gradient, as one measure of the flow. (The horizontal gradient is related to the velocity shear by geostrophy. Other measures could be used, such as comparison of model surface current with estimates from

(a) POP-LR bias: Mixed layer depth.

(b) POP-LR bias: density stratification. Positive=too stratified

(c) POP-LR bias: temp. stratification. Negative=too stratified

(d) POP-LR bias: salinity stratification. Positive=too stratified

(e) POP-LR bias: SST

f) POP-LR bias: SSS

(g) POP-LR bias: SHF. Positive = Up

altimetry and drifter, but the dynamic height estimate is useful in that it also provides a means of comparing the geostrophic flow estimates derived from Levitus and Argo.) The dynamic height measure cannot describe the barotropic part of the flow, but it remains useful as a key component of the stratification budget is the differences in advection between different vertical levels, in turn related to the current shear.

Dynamic height gradients from Argo and Levitus show the basic flow features of the ARC, ACC etc. in the Southern Ocean, with Levitus tending to produce somewhat weaker and broader current estimates. (Fig. 7a, b). For the model differences from Argo (Fig. 7c–e), POP-LR has a a weak gradient relative to Argo along the ARC and ACC, but too-strong gradient to north and south, indicating both weak gradients within the ACC and also some broadening. POP-HR
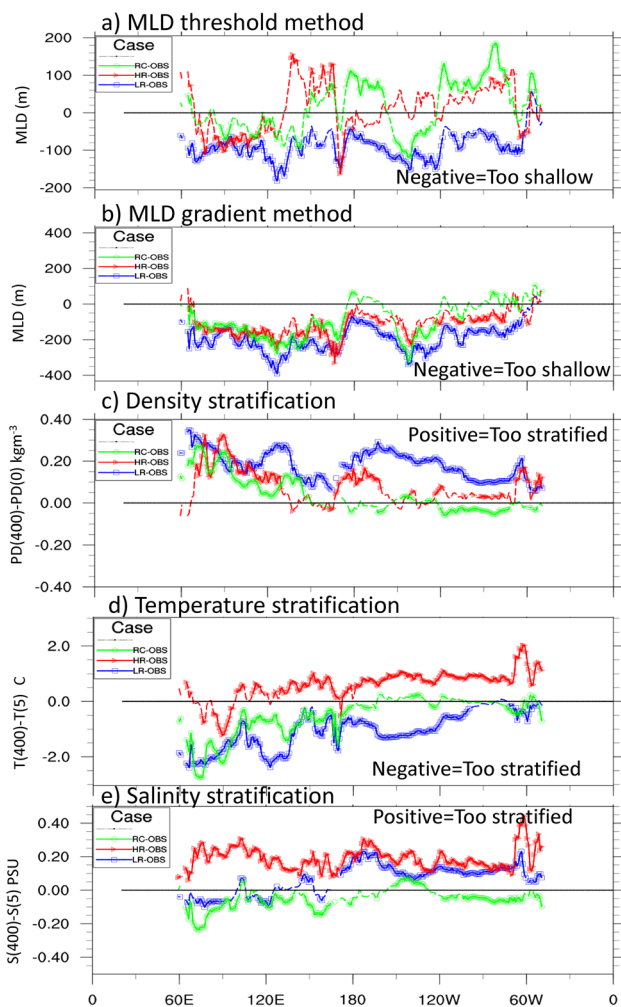
Fig. 5 Model differences from Argo observations averaged in DMB (see legend, where RC = POP-RC, HR = POP-HR, LR = POP-LR). Austral winter averages. Note that mean bias and rmsd of these curves are indicated in Table 2. **a** MLD, defined using the threshold method, **b** MLD, defined using the gradient method, **c** potential density stratification **d** temperature stratification, **e** salinity stratification. Solid lines with symbols denote that differences are statistically significant at 95% according to the *t* test. Dashed portions of lines are not statistically significant

and POP-RC reduce the bias, but some differences with Argo remain. Much of the deficiencies of POP-RC relative to Argo are due to differences between Levitus and Argo (Fig. 7a, b). Despite these differences in derived flow, the next sub-section shows that hydrographic fields (e.g. surface salinity and salinity stratification) from POP-RC agree quite well with Argo especially in the Pacific Ocean.

3.4 Sensitivity of surface fields and stratification to high resolution and improved circulation

The Southern Ocean winter MLD is deeper relative to POP-LR in experiments where circulation is improved either by

using high-resolution in the ocean, or by restoring ocean currents towards observations (Fig. 1). The spatial distribution of the deepest mixed layers in both the POP-HR and POP-RC experiments matches Argo observations better than POP-LR (Fig. 1); however, they both still exhibit a combination of deep and shallow biases in different regions, although some of these differences with observations are not statistically significant (Fig. 5a, see also Supp. Figs. S5b, c, Fig. S6a). The spatial pattern of MLD in POP-RC is similar to those simulated by POP-HR (Fig. 1), but it is broader meridionally, as may be expected from the underlying 1° resolution used in the POP-RC model. In the following we explore how the MLD in the DMB is related to the temperature and salinity stratification, state variables, and air–sea heat fluxes, for both POP-HR and POP-RC.

The overall response in both POP-HR and POP-RC is to destabilize the water column relative to POP-LR in most of the DMB, as seen in the potential density stratification (Fig. 5c). However there are subtle differences in the relative role of temperature vs salinity in controlling this. The temperature stratification in POP-HR and in POP-RC is more unstable than in POP-LR, and for POP-HR it is often more unstable than observed (Fig. 5d). Meanwhile the salinity stratification in POP-RC is more destabilizing than observed in the Indian Ocean but close to observations in the Pacific Ocean, whilst POP-HR is too stratified in salinity relative to observations throughout the DMB (Fig. 5e). This is quantified in more detail in Appendix B using a local Equation of State. Those results suggest that the deeper MLD in POP-HR relative to POP-LR is due to *temperature* in both basins, and is countered by salinity in the Indian Ocean, which has a stratifying effect. In contrast, the destabilizing of density stratification in POP-RC relative to POP-LR is mainly due to *salinity*, with temperature playing a more minor role. These processes are examined in more detail in Sect. 5.

Considering now the surface properties, both POP-HR and POP-RC act to warm the SST relative to POP-LR (Fig. 6b). At most longitudes, the POP-HR SST bias relative to observations is warm but smaller in absolute magnitude than the negative bias of POP-LR (Fig. 6b). Meanwhile the SSS in POP-RC is close to observations, whilst POP-HR exhibits a similar fresh bias to POP-LR in the Pacific Ocean (Fig. 6a). It should be noted, however, that POP-HR has a much better salinity at a depth of 400 m in the DMB (Supp. Fig. S8), implying that most of the error in salinity stratification seen in Fig. 5d in POP-HR is due to surface salinity bias.

The surface heat loss to the atmosphere is stronger in both POP-HR and POP-RC in the DMB relative to POP-LR, often by about 50 Wm⁻² (Fig. 6c). (Many of the differences with observations for the improved circulation experiments are not statistically significant, and in fact differences between POP-LR and observations are also not significant in the eastern Pacific Ocean, a point related to the fact noted above

Table 2 Differences between model simulations and observations in the DMB, time-average for Austral winter

Variables	POP-LR	POP-HR	POP-RC
a) Mean difference of model simulations with observations			
MLD (m), threshold method	− 88	8	14
MLD (m), gradient method	− 189	− 107	− 86
Density Stratification (kg m^{-3})	0.18	0.08	0.04
Temperature Stratification (°C)	− 1.03	0.57	− 0.52
Salinity Stratification (psu)	0.06	0.19	− 0.05
SSS (psu)	− 0.21	− 0.16	0.07
SST (°C)	− 0.63	0.19	0.07
Surface Heat Flux (Wm^{-2})	− 27	6	5
b) Root-mean-square difference of model simulations with observations			
MLD (m), threshold method	95	62	68
MLD (m), gradient method	204	127	130
Density Stratification (kgm^{-3})	0.19	0.11	0.09
Temperature Stratification (°C)	1.22	0.78	0.87
Salinity Stratification (psu)	0.11	0.20	0.08
SSS (psu)	0.24	0.18	0.14
SST (°C)	0.77	0.48	0.38
Surface Heat Flux (Wm^{-2})	40	22	29

(a) The mean difference averaged over the whole of the DMB, (b) the spatial RMS difference, using data at all longitudes in the DMB. See Figs. 5 and 6

that over-stratification in POP-LR in this region is mainly due to erroneous salinity stratification, see also Sect. 5.2.) Since all model simulations use CORE surface forcing, the differences between models in net surface heat flux (SHF) are mainly due to the change in model SST affecting the bulk fluxes. Specifically, the surface latent and sensible heat flux and the upward longwave radiation from the surface are strongly dependent on SST (see Large and Yeager 2012). The air–sea feedback of changes in SHF due to SST in the model in the Austral winter season can be deduced by taking the ratio of the differences between POP-LR and POP-HR of SHF (ΔSHF) and of SST (ΔSST), and is around 40 Wm^{-2} per °C on average in the region of interest (Fig. 6d), which is similar to that found by Large and Yeager (2012). (It should however be noted that this result is strictly dependent on the CORE forcings used in the model simulations, and is thus constrained to give a similar result to that in Large and Yeager (2012) who use the same dataset except for observed SST—other model forcings, and indeed estimates based on observed datasets will give different values, see e.g. Hausmann et al. 2016.)

Consequently, as both POP-HR and POP-RC warm the SST relative to POP-LR (Fig. 6b), they will have larger surface heat loss than POP-LR (Fig. 6c). The consequences of this are explored in the stratification budgets of Sect. 5.

3.5 Comparison of MLD definition

It has been noted before (e.g. DuVivier et al. 2018) that the wintertime density structure in the DMB does not always show a sharp gradient at the base of a well-defined mixed layer—rather, it exhibits weak stratification over a large depth range. As a consequence, there is a large sensitivity of MLD to the calculation method. Using a density threshold of 0.03 kgm^{-3} the Argo MLD is mostly less than 400 m in JAS in the DMB (Fig. 1a), whereas it often reaches 500 m when using the Large et al (1997) gradient method (Fig. 1b). It should be remembered that the threshold method was applied to monthly averaged temperature and salinity, whereas the gradient method was applied to profiles first before averaging.

In contrast, the MLD in POP-LR is much less sensitive to definition (Fig. 1c, d) and it is always much shallower than that seen in Argo in the DMB. The MLDs in POP-HR and POP-RC are more sensitive to definition, and often show larger MLD for the threshold method (e.g. in the S. E. Pacific, Fig. 1e–h). As a consequence POP-HR and POP-RC exhibit a deep MLD bias in the S. E. Pacific, relative to Argo, when using the threshold method, whereas they have a shallow bias when using the gradient method (Fig. 1). These results are summarized in Fig. 5a, b, Supp. Figs. S6a, b and Table 2.

Despite these differences between definitions of MLD, the following general conclusions can be drawn that (a)
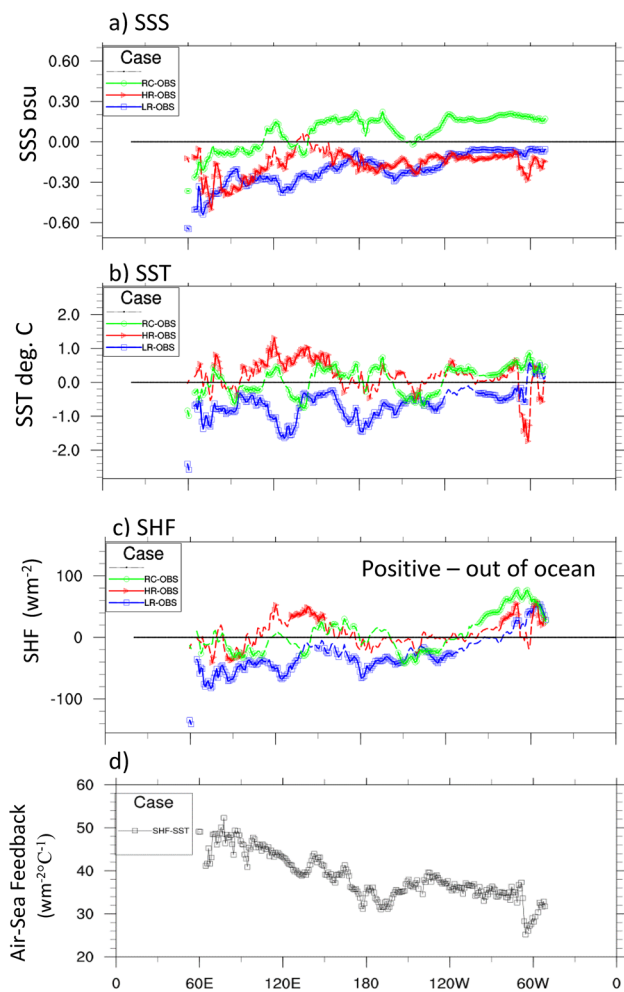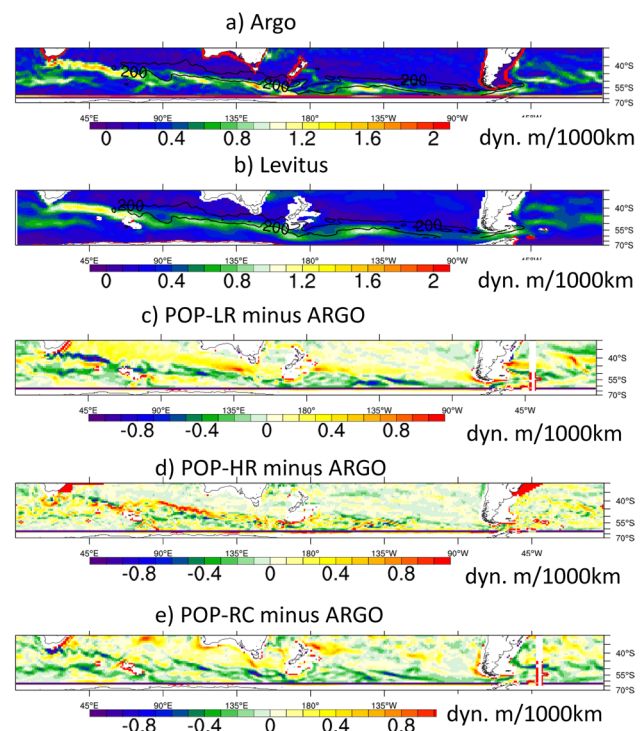
Fig. 6 **a**–**c** As Fig. 5 but for **a** SSS, **b** SST, **c** Surface heat flux. **d** The air–sea feedback in Austral winter derived from POP-HR and POP-LR
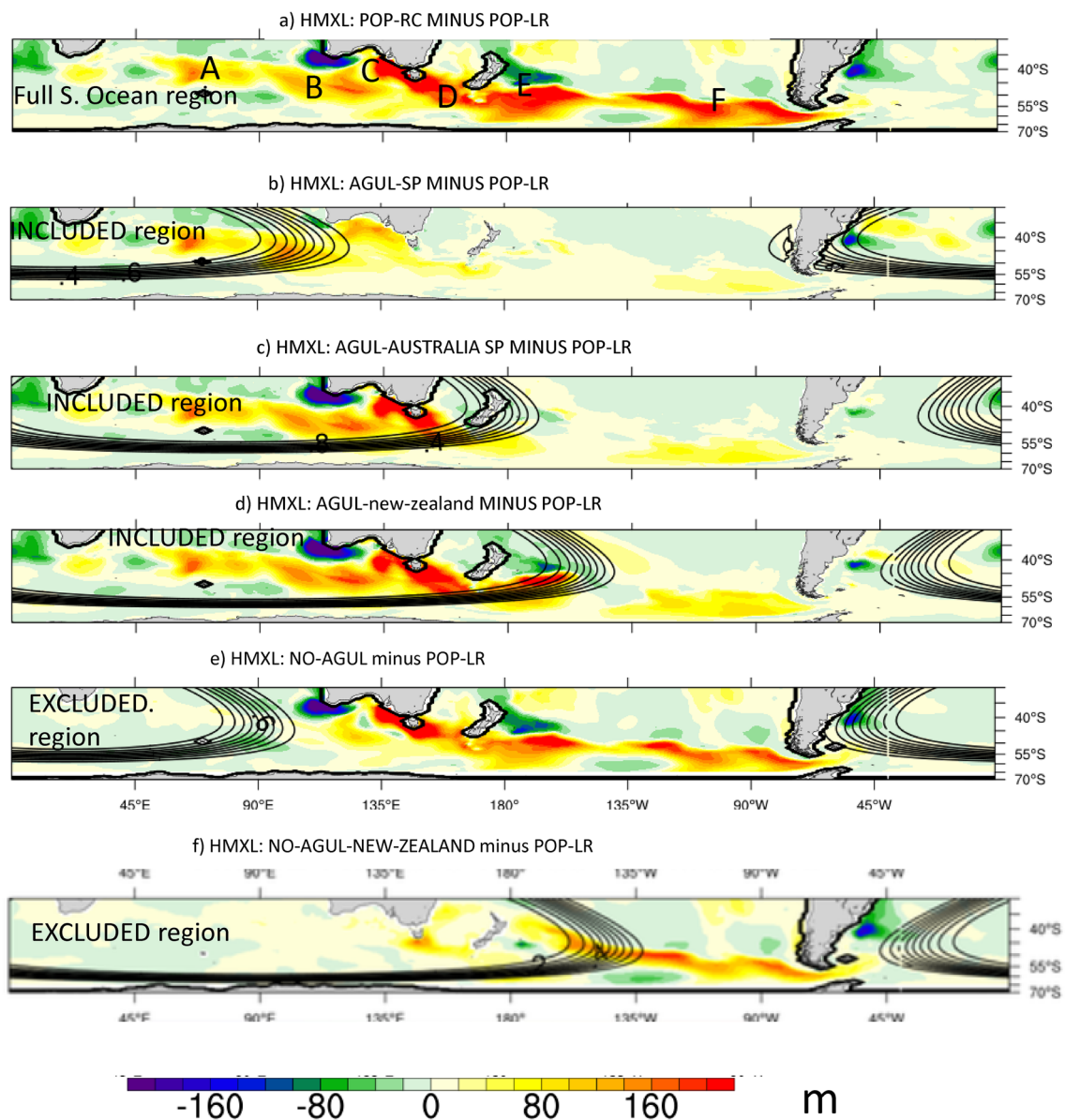
Fig. 7 Magnitude of gradient of time-mean dynamic height (from 1000 m to surface) in dynamic meter per 1000 km, annual mean. **a** From Argo, **b** from Levitus WOA98. **c**–**e** Differences between model and Argo for **c** POP-LR, **d** POP-HR and **e** POP-RC

POP-LR always has a shallow bias in the DMB relative to observations, and (b) POP-HR and POP-RC always deepen the mixed layer relative to POP-LR, in the correct location relative to Argo. For the rest of this paper we use the threshold definition, which is more commonly recognized, but acknowledge that due to the complex density structures, the absolute value of MLD varies between definitions.

4 Local and remote effects of ocean circulation on the DMB: insights from the semi-prognostic simulations

In this section we aim to address whether there are particular key regions in the Southern Ocean where the specified geostrophic oceanic flow and heat/salinity transport of POP-RC leads to a more realistic Southern Ocean DMB than found in POP-LR. This is done via two approaches, (i) by utilizing

regional semi-prognostic experiments, and (ii) by investigating the time evolution of stratification weakening in the semi-prognostic experiments. It will be shown that although there are some remote effects of changes to ocean circulation, much of the response is local, i.e. in order to improve the LR model bias throughout the Subantarctic Zone, the circulation needs to be improved in the entire DMB.

4.1 Regional semi-prognostic experiments

The semi-prognostic method has been applied in different regions of the Southern Ocean to help identify specific regions controlling MLD distribution (Table 1b and Sect. 2.2). The ellipses in Fig. 8b–d) contain the region of the semi-prognostic method, and these are referred to as "Inclusion" experiments. The Inclusion results are differenced with POP-LR to show the local and remote effect of the region (but note the remote regions have the diffuse currents of the 1° model). Large MLD differences *outside* of the ellipse in Fig. 8b–d denote a large *remote* response. Figure 8a shows the results of the full Southern Ocean semi-prognostic experiment POP-RC for comparison. In contrast, in Fig. 8e, f the semi-prognostic method is applied everywhere in the Southern Ocean except the ellipse (referred to here as "Exclusion" experiments.) The runs are compared

a) HMXL: POP-RC MINUS POP-LR

b) HMXL: AGUL-SP MINUS POP-LR

c) HMXL: AGUL-AUSTRALIA SP MINUS POP-LR

d) HMXL: AGUL-new-zealand MINUS POP-LR

e) HMXL: NO-AGUL minus POP-LR

f) HMXL: NO-AGUL-NEW-ZEALAND minus POP-LR

Fig. 8 Results from regional simulations with semi-prognostic (SP) restoring of currents. **a–d** Show Austral winter MLD for experiments minus POP-LR. **a** Is the full S. Ocean case, POP-RC **b–d** Apply the method only in the ellipse shown, tapering the amount of replacement of model density in the hydrostatic equation from 1 (full replacement) to zero (no replacement) within the contours (0.1 intervals). **e–f** show EXCLUSION experiments where the SP method is applied everywhere except in the ellipse shown. **e–f** Show MLD in the EXCLUSION experiment minus that in POP-LR. In **a**, regions referred to in text as A–F are labelled. See also Table 1b. Results are for first 18 years of the runs, all starting from same initial condition

against POP-LR and so now large MLD differences *outside* of the ellipse in Fig. 8e–f implies that there is a sizeable response that is independent of the ellipse region, i.e. more *local*. This is another method of determining the influence of an upstream region on remote downstream regions: but in this case the remote region has realistic currents. All the experiments are listed in Table 1b. For reference in the discussion below, locations A to F of enhanced MLD difference are labelled on Fig. 8a for convenience.

The effect of the ARC region is shown in Fig. 8b, e. Firstly, we note that MLD within the ARC system (e.g. near point A) is almost totally determined by applying the semi-prognostic method in that region alone (compare Fig. 8a, b and confirmed in Fig. 8e). Secondly there seems to be a very small influence of the ARC system on the MLD in the Pacific Ocean (compare Fig. 8a, b), again confirmed in Fig. 8e. However, in the ACC region in longitudes 90° E to 150° E (e.g. around point B), the ARC system does have

Fig. 9 Temporal evolution of MLD differences between POP-RC and POP-LR in the Austral winter season (JAS). **a** Year 1, **b** average of years 3 and 4, **c** average of years 5 and 6
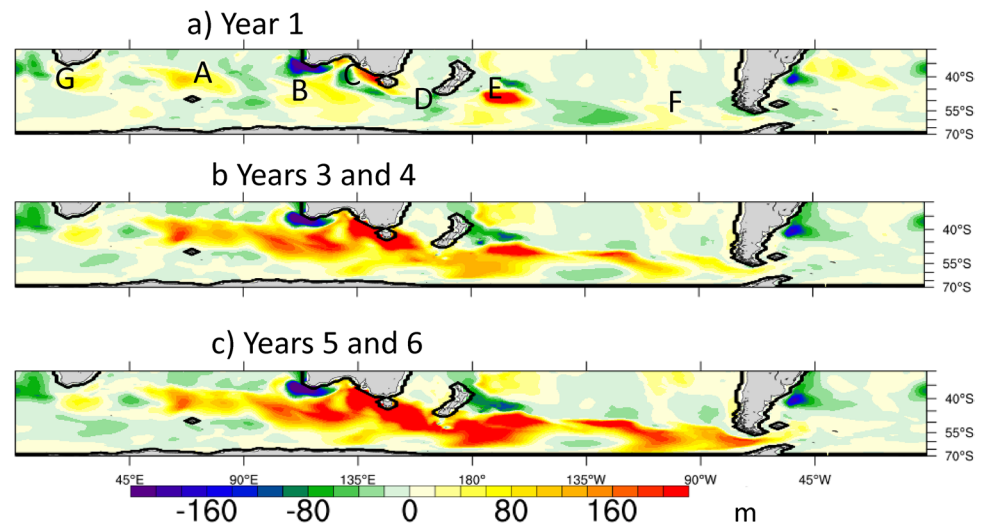
an influence (seen most clearly by comparing Fig. 8a, e in that location). This implies that the MLD in the ACC south of Australia is significantly influenced by the entire current structure of the southern Indian Ocean, including the ARC system.

The shift of deep mixed layers from the south-west coast of Australia to the south-east coast (Fig. 8a, b, c, e: west to east of point C) is a local effect—this is due to a strong extended eastward Leeuwin Current off the south coast of Australia in POP-RC (and POP-HR) that is not present in POP-LR. The extended Leeuwin Current, also known as South Australian Current, was recently detailed by Wijeratne et al. (2018). These coastal processes are not discussed further as the semi-prognostic method is not applied directly at the nearest 2 grid points to the coast, and the WOA98 database may not be sufficient to give a realistic representation of flow in these regions.

Next we aim to distinguish local and remote causes of MLD deepening in the Pacific Ocean east of New Zealand. Applying the semi-prognostic method in the whole Indian Ocean and Tasman Sea does not significantly impact MLD east of New Zealand (Fig. 8c). Only when the ellipse is expanded eastwards to include the region around location E does the MLD deepen in that same region—implying the MLD changes around E are strongly locally controlled (Fig. 8d). In that same experiment, the MLD also deepens in the South–East Pacific by 80 m or more (Fig. 8d) but the pattern does not strongly resemble that of the full semi-prognostic experiment POP-RC (Fig. 8a). Further, if the Exclusion method is applied to a similar shaped ellipse covering Indian Ocean, Tasman Sea and region east of New Zealand (Fig. 8f), the MLD difference still reaches 150–200 m in the South East Pacific. We conclude that the MLD in the SE Pacific is significantly influenced by both the local currents

in the S. E. Pacific, and to a lesser extent currents east of New Zealand, but not substantially by the ARC system.

Note finally that the locations A to F in Fig. 8a are also roughly consistent with where POP-HR has deeper MLD than POP-LR (Supp. Fig. S9) but with some differences—point B is not so prominent in POP-HR, the dipole around E is on a smaller scale in POP-HR, and there are differences in the detail of the MLD difference around point F. However, the general consistency between POP-RC and POP-HR at these locations suggests robustness of the effect of improved circulation.

4.2 Temporal development of MLD differences due to semi-prognostic method

Another method to analyze the roles of local vs upstream control of deep MLD is to examine the evolution in time of differences between the POP-RC and POP-LR experiments, both initialized on Jan. 1st from the same initial condition. Figure 9 reveals that many of the key deepening regions) already appear in the first Austral winter season (Fig. 9a) and are mostly fully developed after ~5 to 6 years (Fig. 9b, c) as can be seen by comparing with the longer-term (18-year) difference shown in Fig. 8a). Referring to the locations A–F used for Fig. 8a (and repeated in Fig. 9a), the following can be deduced:

- locations A and B in the Indian Ocean and the dipole at location E east of New Zealand are already notable in year 1, and they continue to deepen through year 6, suggesting local forcing.
- The MLD deepening at location D (south-west of New Zealand) emerges later, after 3 years, indicating the pos-

Fig. 10 Hovmoller diagrams of POP-RC minus POP-LR anomalies averaged in the DMB. **a** Sea surface salinity (SSS), **b** potential density (PD) at 200 m minus that at 400 m. **c** PD at 5 m minus that at 200 m. Arrows show propagation behavior, see text. Letters correspond to Fig. 8a
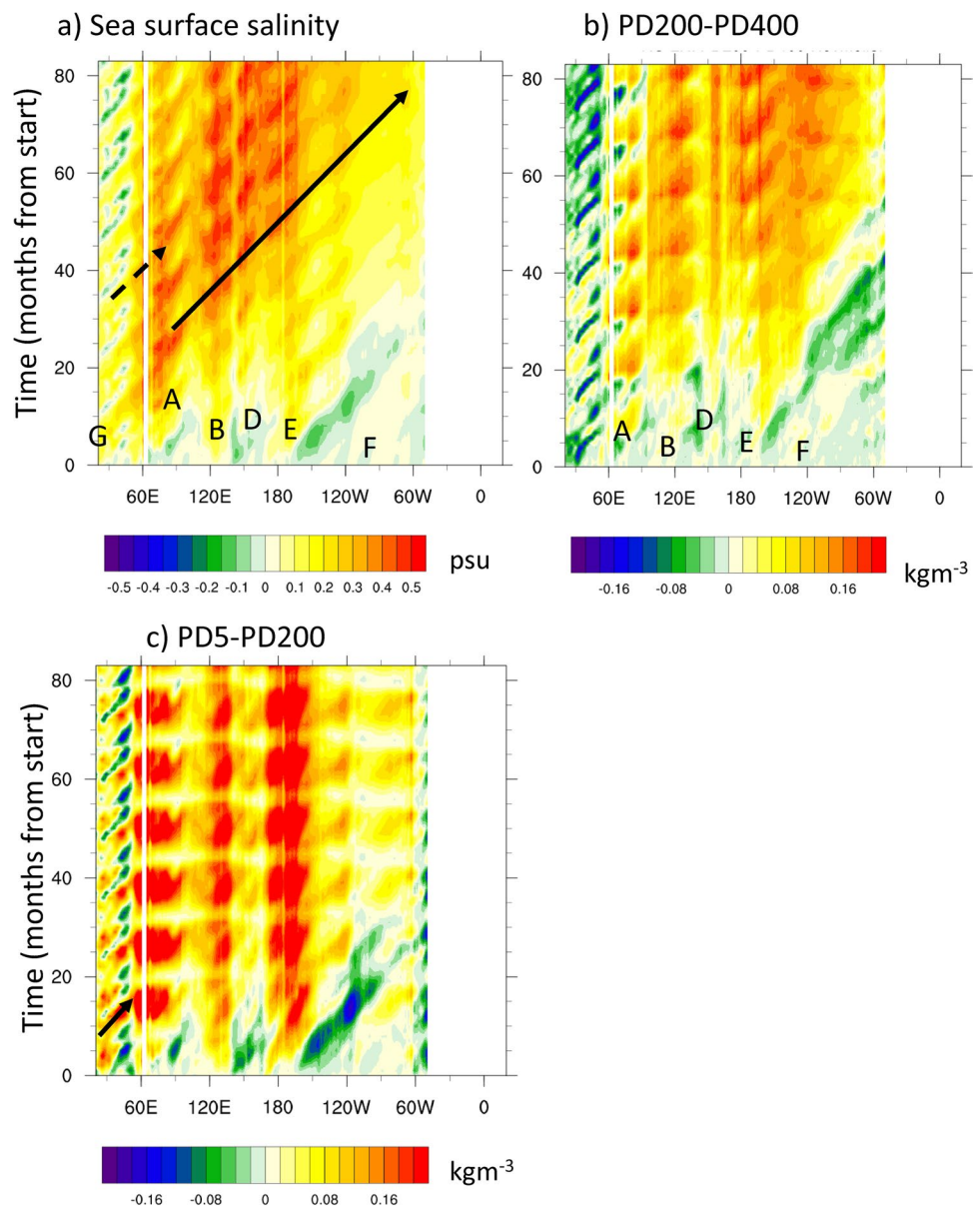
sibility of a remote response to upstream deepening in earlier years.

- Around location F in the S.-E. Pacific, the deepening is the slowest to emerge, but the spatial pattern of deepening is evident, albeit very weak, in most of the SE Pacific in year 1, suggesting it is a combination of local and remote upstream forcing.

- In the Agulhas retroflection region (point G), deepening is immediately seen in year 1 but does not grow in time, possibly because a destabilizing tendency of salt is eventually cancelled out by stabilizing temperature tendency, as shown by the heat and salinity budgets of Sect. 5.

For a more detailed inspection of the temporal evolution, Hovmoller diagrams have been created for an "extended DMB region" which includes the DMB defined above (where MLD in Argo exceeds 200 m in winter) and also includes the region upstream of the DMB, in this case 35° S to 41° S, 10° E to 60° E. (The latter region was chosen after inspection of individual maps of anomalies of SST and SSS in the first year showing propagation from the Agulhas retroflection to 60° E within this latitude range—see e.g. Supp. Fig. S10). Hovmoller diagrams for 3 key variables are displayed in Fig. 10.

The Hovmoller diagram of differences in SSS between POP-RC and POP-LR, referred to as ΔSSS (Fig. 10a), reveals a number of interesting features:

(i) Clear evidence of eastward propagation (e.g. black arrow)

(ii) Some anomalies also generally get stronger with time *in a fixed location.*

(iii) Centers of action like A, B, D, E, and possibly F emerge early. Even in the first month there is evidence of a (weak) anomaly.

(iv) At location F, although there is a local early response in the first two years, the anomalies only get strong when upstream signals reach F, later in the record.

(v) There is a connection between the upstream (Agulhas retroflection) region and the DMB (i.e. signals propagate between the two- see e.g. short black dashed line, also the solid black line is preceeded by anomalies in the western box) but anomalies in the DMB can occur before the Agulhas signal reaches them. This suggests the Agulhas signal is reinforcing but not creating the downstream anomalies, consistent with the regional semi-prognostic results.

(vi) There is a suggestion that the anomalies are carried downstream by the ACC. This is based on the fact that the solid black arrow in Fig. 10a covers ∼ 210° longitude in 50 months, ∼ 4.2°/month, equivalent to 0.13 ms^{-1}, whilst typical zonal velocities in the ACC in POP-RC are 0.1 to 0.2 ms^{-1} (Supp. Fig. S11).

The deep stratification of potential density (PD_{deep}, see Sect. 2.4) is investigated next. Anomalies of PD_{deep} (i.e. differences between POP-RC and POP-LR, referred to as ΔPD_{deep}, where positive values indicate that POP-RC has a weaker stratification) can be more easily tracked than MLD through all months of the year, as it is not affected by the summer seasonal thermocline so much and hence has a much smaller seasonal cycle than MLD.

The Hovmoller diagram for ΔPD_{deep} closely resembles that for SSS (and to a lesser extent, that for SST and surface heat flux, not shown) for longitudes east of 60° E (Fig. 10b). Similar features to A, B, D, E, F in the SSS record are seen in ΔPD_{deep}. The eastward propagating signals and the annual cycle are also apparent. The main difference between ΔPD_{deep} and SSS occurs west of 60° E. Here, we know from Fig. 1 that MLD is mostly shallower than 200 m in POP-RC and POP-LR so that ΔPD_{deep} is not a relevant quantity to MLD at these locations. If we use instead the potential density difference between 5 and 200 m ($PD_{shallow}$), we do indeed find that anomalies of weak stratification (positive values) are present west of 60° E and propagate eastwards towards the DMB (Fig. 10c, see example black arrow).

All of the above findings were corroborated by analysis of Hovmoller diagrams of ΔPD_{deep} from the *regional* semi-prognostic experiments, which allow for tracking of localized ΔPD_{deep} features, as described in the Supp. Material (see caption of Supp. Fig. S12).

In Sect. 5 separate budgets for salinity and temperature stratification are presented, so in anticipation it is useful to look at the time evolution of salinity difference between 200 and 400 m, and similarly for temperature. The results show that the salinity stratification becomes positive (destabilizing) throughout the DMB within the first 3 years or so (Fig. 11a), whilst the temperature stratification has a mixture of negative (destabilizing) and positive (stabilizing values). The processes responsible for this are examined in Sect. 5. Next, the temperature and salinity stratifications are converted into equivalent changes in potential density stratification using the local EOS of Appendix B. This reveals that salinity is the major contributor to changes in density stratification (compare salinity contribution Fig. 11c with full density change Fig. 10b) whilst temperature plays a more mixed and weaker role (compare Figs. 10b, 11d).

5 Ocean heat and salinity stratification budgets

In order to further understand the changes in stratification discussed in Sects. 3 and 4, two sets of heat and salinity budgets are applied.

In Sect. 5.1, for the comparison of low resolution and high resolution models, a time average of the budget terms is applied for the annual mean steady state. As POP-HR has weaker stratification mainly due to temperature changes (Sect. 3.4), only the temperature stratification budget is considered. Then, in Sect. 5.2, for the comparison of semi-prognostic runs with low resolution, a time-average of budget terms for temperature and salinity stratification is shown together with analysis of the initial evolution of differences between simulations.
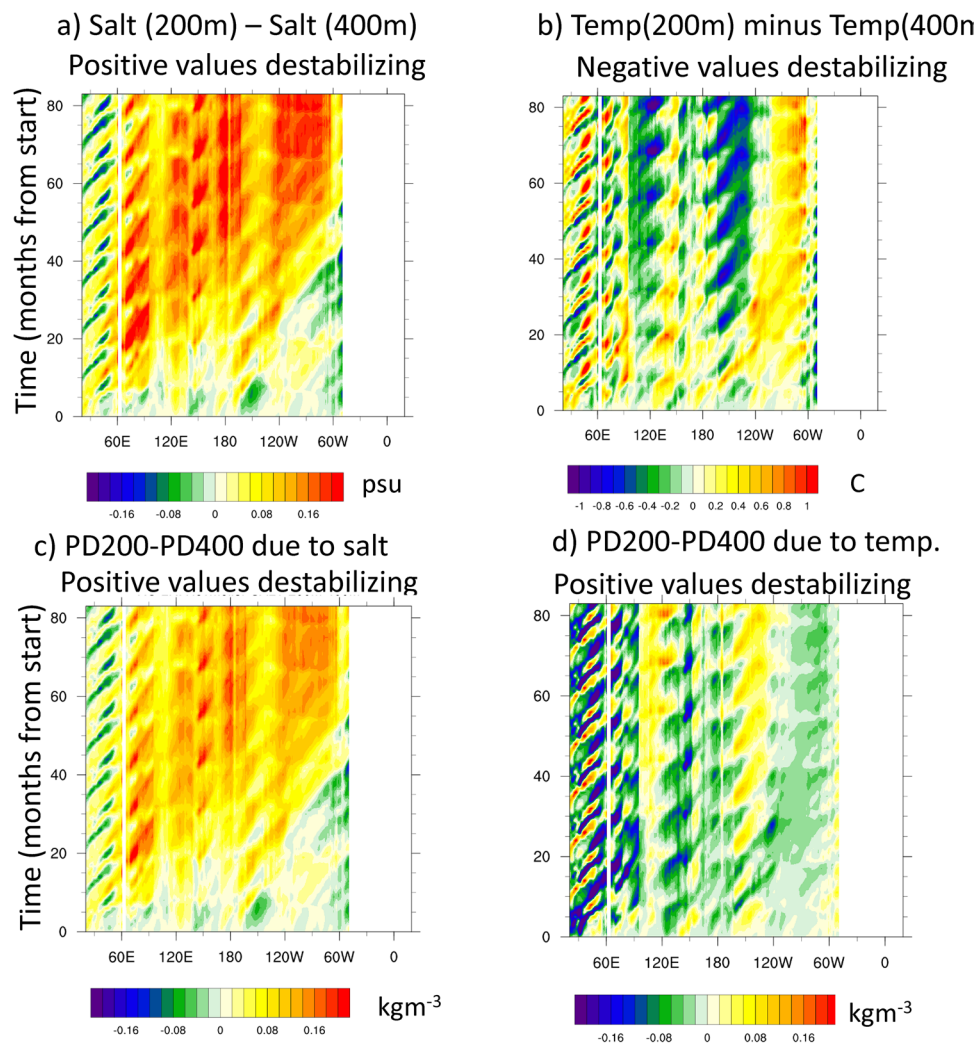
It will be shown that in POP-HR, the enhanced air–sea heat loss is the dominant factor leading to weakened stratification relative to POP-LR, whilst enhanced salinity advection in the upper ocean into the DMB governs the stratification weakening in POP-RC. As the air–sea heat loss effect in HR is a feedback due to warmer SST, in turn due to heat advection, we see that improved tracer advection (*in turn due to improved circulation*) is the underlying factor in both cases.

5.1 Temperature stratification budget and sensitivity to model resolution

When a heat budget is performed to a fixed depth just below the deepest mixed layer depth in the annual cycle, called H here, the main terms of (1) are tendency (storage), resolved 3D advection, convergence of parameterized (horizontal) transport and surface heat flux. Further, when computing an annual mean budget where the ocean is in approximate steady state, the tendency becomes relatively small, so that the last 3 of these terms balance. Recalling our definition of

Fig. 11 **a**, **b** As Fig. 10b but for the salinity and temperature stratification respectively. **c**, **d** The equivalent changes in potential density stratification assuming a local EOS

a) Salt (200m) – Salt (400m)
Positive values destabilizing

b) Temp(200m) minus Temp(400n
Negative values destabilizing

c) PD200-PD400 due to salt
Positive values destabilizing

d) PD200-PD400 due to temp.
Positive values destabilizing

OHFC as equal to resolved advection for the high resolution model, and equal to resolved advection plus convergence of parameterized transport for the low resolution model, it follows that the annual mean heat budget is a primary balance between surface heat flux and OHFC.

This argument can be taken a step further for the "vertically averaged stratification budget" for T_{strat} (see definition in Sect. 2.5). Here the heat budget at the depth H is subtracted from the depth-averaged budget to depth H. As surface heat flux does not affect the budget at depth H, and the interior diffusion is typically small at that depth, the primary balance at that depth is between tendency and OHFC, and again for an annual mean where the tendency is small it follows that the net OHFC at depth H is near-zero also. (In practice, this is manifested by a near cancellation of resolved advection and parameterized transport in POP-LR, whilst in POP-HR there is a weak, patchy advection on eddy scales due to the simulation being not perfectly steady state, but there is no large-scale advection.) Thus in an annual mean case the budget of the stratification (defined by 4) is very

close to the more traditional depth-integrated budget to depth H (2). (Note that this does not hold for seasonal means where the tendency is a significant term, or for differences between simulations that diverge from an initial state.) The above assertions have been confirmed in full heat budgets of POP-HR and POP-LR, where all the heat budget terms were known (see Supp. Figs S13-S14).

From the above arguments, the only information needed to know the vertically averaged stratification budget for temperature in the annual mean to a depth immediately below the deepest mixed layers is the surface heat flux, as the OHFC is approximately equal and opposite. As the observed stratification to depths of 400 m or so is weak in the DMB all year round (Fig. 3), we will use this annual mean stratification budget to help interpret why model solutions and observations differ.

The annual mean net surface heat flux from the Trenberth and Fasullo (2017) observational analysis, and in POP-LR, POP-HR and POP-RC simulations, is shown in Fig. 12. (Other observed products are shown in Appendix A.) Using

Fig. 12 Annual mean net surface heat flux, with positive values denoting ocean heat loss. **a** Trenberth-Fasullo 2017 estimate, **b** POP-LR, **c** POP-HR, **d** POP-RC, using same color bar. Contours of 200 m, 400 m winter MLD from Argo are overlaid
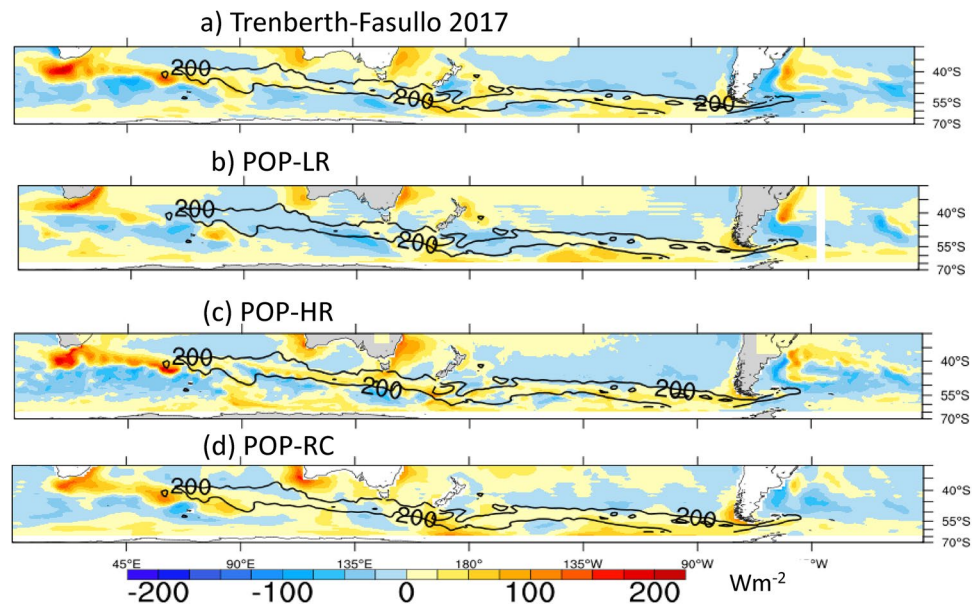
the overlaid 200 m contour of Argo winter MLD as a reference, it can be seen that a strip of air–sea heat loss (positive values) coincides with the DMB in observations, POP-HR, and POP-RC, but in POP-LR there is mainly air–sea heat gain (negative values) in the Indian Ocean DMB and a substantial part of the Pacific Ocean DMB. (For the Indian Ocean this point was recognized by Lee et al (2011)).

The quantitative differences between the models and the Trenberth and Fasullo (2017) product are highlighted in Supp. Fig S15). It is shown there that POP-LR exhibits a strip of insufficient heat loss in the deep MLD region whilst POP-HR and POP-RC are closer to the observations but with some positive bias in heat loss in POP-HR.

As discussed above, the OHFC integrated to a depth immediately below the deepest mixed layer is approximately equal and opposite to the air–sea heat flux in the annual mean, and so Fig. 12 can also be interpreted as the OHFC term, if this time we define positive values as heat gain in the upper ocean (stratifying). Thus we see OHFC has a stratifying influence in the region of deep mixed layers in all cases except POP-LR, which has insufficient heat gain due to advection. This was confirmed in full heat budgets (Supp. Figs. S13, S14).

The above results lead to the following interpretation: a warm upper ocean and SST is maintained in the regions of deepest mixed layers by OHFC: and the warm SST gives rise to large air–sea heat loss in the same region via the air–sea feedback. In the annual mean steady state these terms are in close balance, but Sect. 5.2 considers cases where simulations diverge from an initial state, such that we can diagnose the influence of the different budget terms on the total tendency of stratification.

5.2 Sensitivity of heat and salinity stratification budget to improved ocean circulation

For both POP-LR and POP-RC, the "vertically averaged stratification budget", for T_{strat} and S_{strat}, defined in Sect. 2.5, is computed. The difference in model simulations, defined as ΔT_{strat} and ΔS_{strat}, is analyzed, using POP-RC and POP-LR. As these experiments were initialized from the same initial condition (see Table 1, and in this section we refer to POP-LR-EXT as POP-LR, see Sect. 2.2), the average of budget terms over the record can be used to interpret these differences.[5] The annual mean is analyzed, as discussed above. The depth of integration is 400 m, deeper than most of the deepest mixed layers in these experiments, except in some isolated spots in POP-RC. Note that for temperature, the budget is converted into an equivalent heat budget in units of Wm^{-2}. The budget is an average from the first 7 years of the simulations.

As in the annual average heat budget of Sect. 5.1, the main balance in the ΔT_{strat} budget is between OHFC and surface heat flux (Fig. 13b, c). However, as we are now considering how the two models diverge from an initial condition, there is a net tendency term (Fig. 13a), which is significantly smaller than either the advection or heat flux (note change of color bar range). The tendency has negative values (destabilizing) in many but not all of the

---

[5] Strictly, differencing the time-average of budget terms allows one to interpret the processes leading to differences in the instantaneous state at the end of the runs. This could be subject to transient, natural variability. An alternative method, the so-called "double-time-average" approach of Oerder et al. (2015), was also applied to smooth-out the natural variability. The results of both methods were very similar and the single-time-average is used here.

Fig. 13 Time-average of temperature stratification budget terms, for POP-RC minus POP-LR. Annual mean. Overlaid contours are MLD difference at 100 m intervals. **a** Stratification tendency term, **b** total advection (OHFC) term, **c** vertical diffusion including surface heat flux. Sign convention: negative values in temperature stratification budget are destabilizing
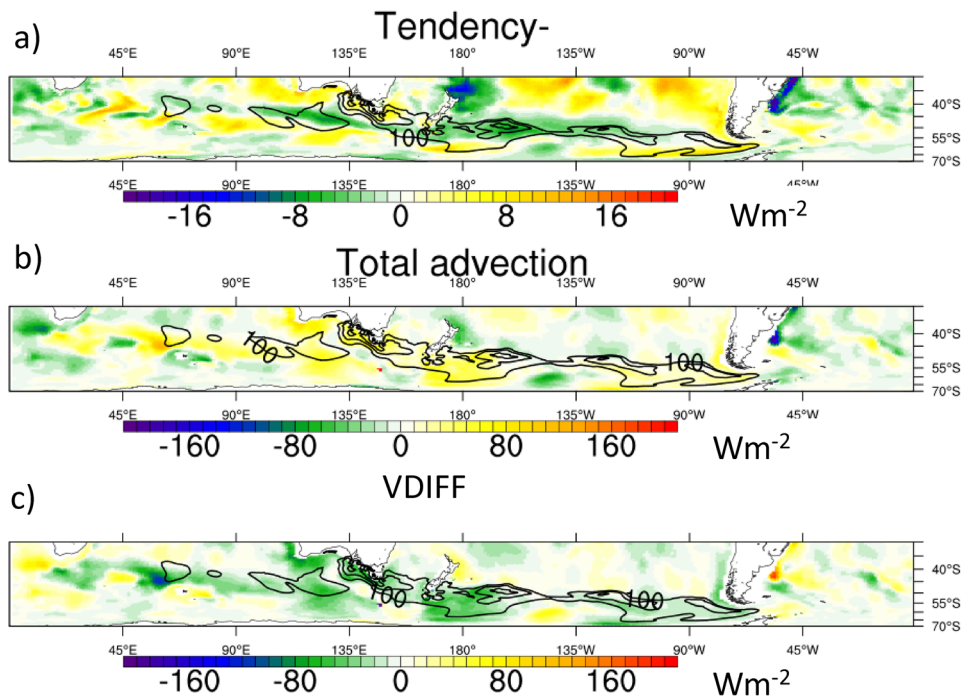
Fig. 14 Time-average of salinity stratification budget terms, for POP-RC minus POP-LR. Annual mean. Overlaid contours are MLD difference at 100 m intervals. **a** Stratification tendency term, **b** total advection term, **c** vertical diffusion including surface freshwater flux. Overlaid contours are MLD difference at 100 m intervals. Sign convention: Positive values in salinity stratification budget are destabilizing
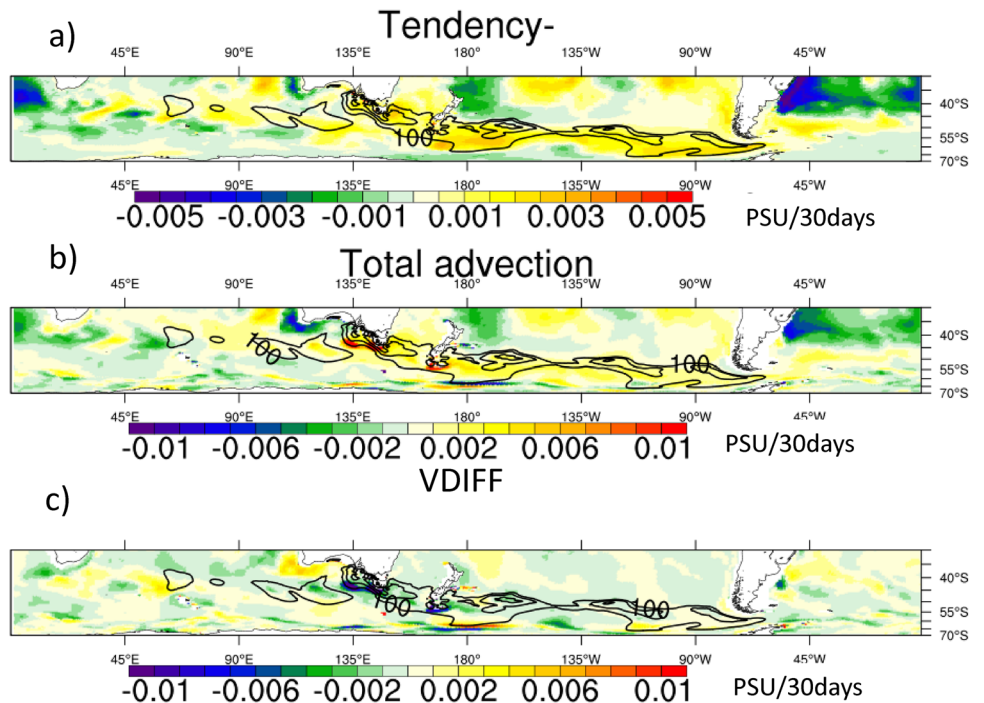
regions where POP-RC has a deeper MLD than POP-LR (overlaid contours are MLD differences between the experiments, referred to as ΔMLD). Comparison with the individual budget terms (Fig. 13b, c) shows that the tendency of ΔT_{strat} has the same sign of the surface flux in most of those regions, whereas it is countered by advection. However, in the S. E. Pacific and around the Australian coast,

the tendency of is of the wrong sign to explain mixed layer deepening. In general, the sign of the tendency changes in Fig. 13a is consistent with the results of the time-evolution of temperature stratification, Fig. 11b.

Turning now to the vertically averaged salinity stratification budget for ΔS_{strat} the tendency of ΔS_{strat}, shows positive values in much of the Southern Ocean, especially in

the DMB (Fig. 14a). In particular it is of the correct sign to explain destabilization in the S. E. Pacific and around the Australian coast where ΔT_{strat} had the wrong sign (Fig. 13a). The salinity destabilization is mainly driven by changes to salinity advection (Fig. 14b) as the vertical diffusion contribution is generally weak, except at some locations south of Australia where the MLD in POP-RC extends beyond 400 m depth so that interior diffusion is important there (Fig. 14c). Once again, the sign of the tendency changes in Fig. 14a is consistent with the results of the time-evolution of salinity stratification, Fig. 11a.

5.3 Early processes in heat and salinity stratification budget

The budget results listed above are an average over multiple years and mix the initial development of differences between simulations with equilibrated processes. More insight can be found from analysis of the initial development alone, for example in the first months and first year. For example, inspection of the depth-averaged salinity budget (to 400 m) for the first month revealed that changes in salinity between POP-RC and POP-LR were driven by advection, and in particular horizontal advection by the monthly-mean flow dominated (Fig. 15). Surface fluxes, vertical advection, parameterized transport, all played a negligible role. However sub-monthly resolved advection (difference between the resolved advection computed online, and that computed from monthly-mean fields[6]) did play a role and helped in the salinification of the DMB (Fig. 15h).

Further it was found that if the horizontal advection term was computed using the flow from POP-RC and the salinity from POP-LR, it was almost identical to the full POP-RC advection, meaning that the flow anomalies are driving changes in the first month (compare Fig. 15e, i). In essence, these results show that initially, horizontal flow changes due to the semi-prognostic method act on the existing tracer gradient (of salt, temperature) of the control simulation to give rise to advection anonalies that force changes in the salinity field. The same findings were found for the salinity *stratification* budget [i.e. for S_{strat}, see (4)] in the first month (not shown).

After a few more months, the salinity budget gets more complex, as the parameterized transport responds to the changes initially driven by resolved advection so that both play a significant role (Supp. Fig. S16.) Vertical advection and surface fluxes still play a minor role, however.

Regarding the *temperature* stratification budget in the first year, it displays a similar behavior to salinity, in that horizontal advection of temperature drives the main changes in temperature between POP-RC and POP-LR (not shown). In the first year, the surface heat flux feedback plays a weak role.

Further examination of the stratification budgets in subsequent years (not shown) revealed similar behavior, but with the surface heat flux feedback growing in importance so that it eventually overrides the magnitude of the advection to give rise to an overall negative tendency in the DMB (see Fig. 13).

To summarize, the following may be concluded on the time evolution of the changes in stratification between POP-RC and POP-LR:
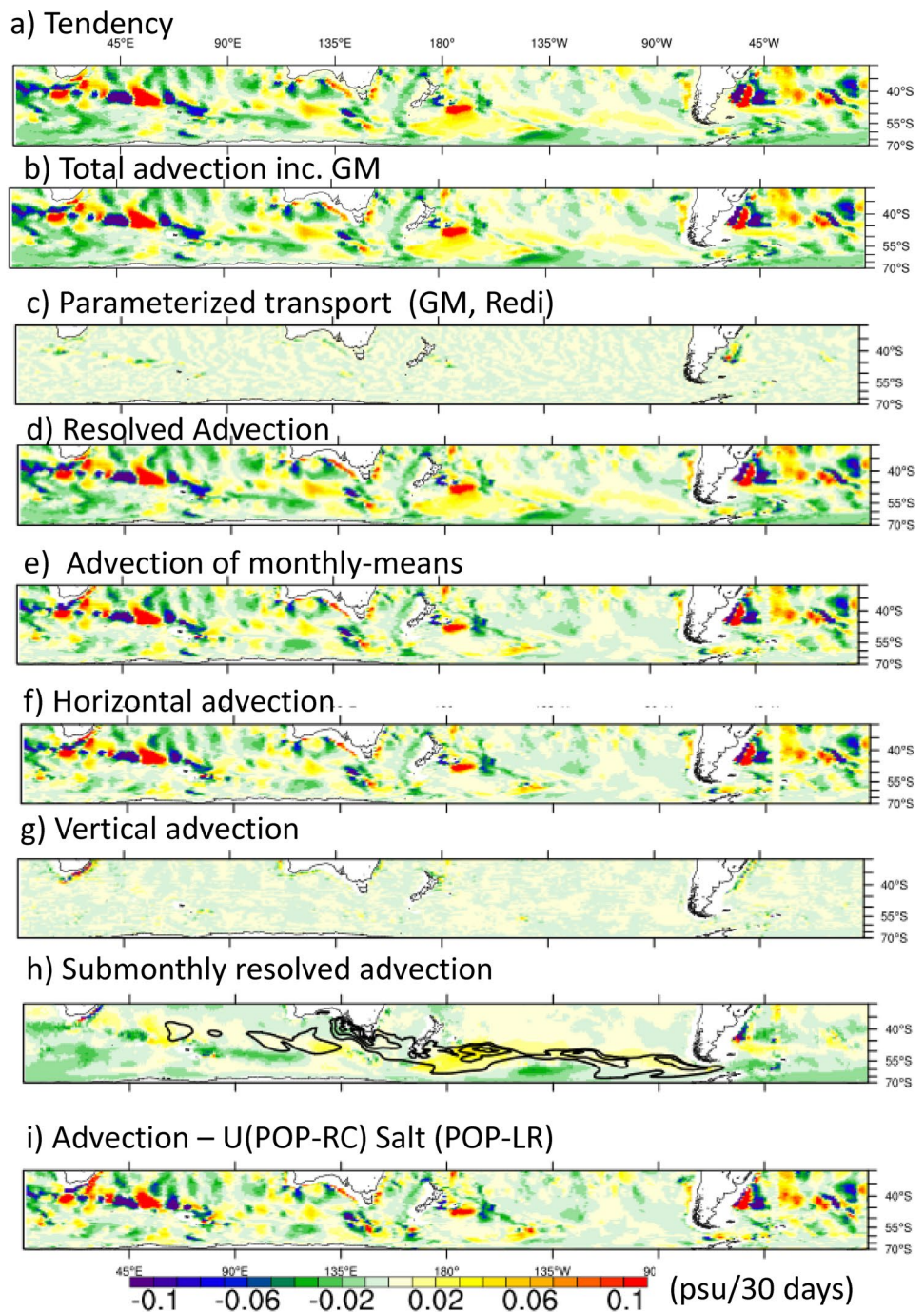
i) Initial destabilization is driven by salinity, whilst temperature applies a stabilizing influence.
ii) In the first one-two months, the differences are driven by resolved advection. Surface fluxes, interior mixing and GM parameterization are negligible.
iii) Horizontal advection completely dominates over vertical advection, meaning that changes are driven by horizontal currents flowing across horizontal temperature or salinity gradients.
iv) In the first two months the changes in horizontal advection are mainly due to changes in flow (i.e. current anomalies). Only later does advection of temperature or salt anomalies become important.
v) By the end of the first year other processes such as surface fluxes (for temperature but not salinity), and GM parameterization become important, but do not dominate.
vi) Overall, in the first year, salinity processes dominate destabilization, but in later years temperature is also important to destabilization, as the air–sea heat loss feedback becomes large and comparable to advection.

6 Discussion

6.1 Problems in simulating the ocean circulation at low ocean resolution

This study shows that the ocean circulation exerts a controlling influence on the air–sea heat flux, upper-ocean density stratification and the winter MLD in the Subantarctic Zone. As low resolution models (~ 1°) are still the main contributors to CMIP experiments (exceptions are the HighResMIP experiments, e.g. Gutjahr et al. 2019), a relevant question is whether changes can be made to low-resolution simulations to improve the circulation and thereby increase deep mixing and the related uptake of heat and greenhouse gas?

---

[6] For the budget at the single level H, the sub-monthly advection computed this way as a residual was negligible. This indicates that a) the sub-monthly advection mainly plays a role in the upper 400 m depth-average, and b) errors in computing monthly advection are likely very small.

Fig. 15 Salinity budget for first month of simulation, POP-RC minus POP-LR. Depth average to 426 m. **a**–**h** are for POP-RC minus POP-LR. **a** Tendency of salt. **b** Resolved plus parameterized transport. **c** Parameterized transport. **d** Resolved advection accumulated every timestep. **e** Resolved advection based on monthly mean current and salt, **f** as **e** but horizontal only, **g** as **e** but vertical component only, **h** submonthly resolved advection **i** as **e** but replaces POP-RC advection with advection based on currents from POP-RC and salinity from POP-LR. Surface flux/vdiff terms are not shown and are negligible in this case

a) Tendency

b) Total advection inc. GM

c) Parameterized transport (GM, Redi)

d) Resolved Advection

e) Advection of monthly-means

f) Horizontal advection

g) Vertical advection

h) Submonthly resolved advection

i) Advection – U(POP-RC) Salt (POP-LR)

(psu/30 days)

The transports of heat and salinity in a low-resolution simulation are determined from a combination of resolved and parameterized components. The relative success of the semi-prognostic method indicates that the resolvable circulation, i.e. the current structure, is the component in most need of correction rather than the parameterized components in order to improve MLD estimates.

The currents in POP-LR are impacted by several factors: coupling with the atmosphere, nonlinear momentum advection, Coriolis accelerations, pressure gradient, and parameterizations of eddy momentum transport which, in the POP model, amount to viscous mixing. All of these factors may be impacted by unresolved processes that are not currently parameterized in POP-LR (e.g. Li and Lee 2017; Bachman 2019). Of these factors, the pressure gradient is the obvious culprit since replacing the pressure gradient via the semi-prognostic method improves the circulation, but there are few methods for altering the pressure gradient in a self-contained model. The stochastic parameterization of the pressure gradient developed by Brankart (2013) could

perhaps play a role here. An alternative way to improve the resolved circulation could be to use higher-accuracy numerical methods for computing nonlinear momentum advection. Regions like the ARC where the large-scale current retroflects in the space of just a few model grid points might benefit from improved numerical methods.

A similar improvement in the circulation might be achieved through grid refinement, either locally in the Southern Ocean (e.g., Ringler et al. 2013) or globally as in POP-HR. However, it is not fully understood how sensitive the circulation is to the numerical method or grid resolution, and previous studies suggest that substantial improvements can be obtained for resolutions substantially coarser than in POP-HR, with positive implications for the MLD in the Subantarctic Zone (e.g., Lee et al. 2011). Further, it is not fully understood why the circulation, and thereby MLD, improves with resolution. However it seems likely that bathymetric resolution may be important for improving the circulation given the importance of topography in governing many aspects of the Southern Ocean dynamics, including standing meanders, flow convergences, eddy energetics (e.g., Thompson and Sallée 2011; Tamsitt et al. 2016).

The reviewers of this paper asked whether the semi-prognostic method may be viewed as having the same effect as a parameterization. We would argue against seeing the prognostic method as an *eddy* parameterization. Consider an ocean simulation performed with the semi-prognostic method but with no additional mesoscale parameterization. In the Southern Ocean the mean overturning will be somewhat realistic but there will be no eddy compensation of the overturning, which is an important component of the overturning (P. Gent, pers. Comm. 2019, Gent 2011).

If a parameterization for the resolved momentum were available that had the same effect of the semi-prognostic method (i.e. improving the resolved circulation), then the semi-prognostic method could be thought of as acting like a parameterization. One such parameterization is that by Brankart (2013), mentioned above, which has recently been refined by Stanley et al. (2020). However this only represents the improvement of one aspect of the dynamics, namely the errors arising from non-linearity of the EOS.

6.2 PV and mode waters

Previous work has noted that biases in winter MLDs in the DMB, similar to those discussed here, are associated with biases in Subantarctic Mode Water formation and export to the subtropical thermocline (e.g., Weijer et al. 2012; Sallee et al. 2013). In particular, biases in winter MLDs in the DMB are two-way coupled to biases in the circulation due to the link between the planetary potential vorticity ($PV = fN^2/g$) and the subtropical gyre circulations (e.g., Rhines 1986), where f is the local Coriolis frequency, g is the acceleration

due to gravity, and N is the buoyancy frequency. As noted before by Weijer et al. (2012), Subantarctic Mode Water in a low resolution model like POP-LR is significantly more stratified and less voluminous and on a shallower density surface than in an observed WOCE hydrographic section in the same season (February 2016 section at ∼ 90° E, see acknowledgements for details, c.f., Fig. 16b, c). In the high-resolution POP-HR, the mode water is more voluminous and less stratified than POP-LR, but still less denser and less voluminous than in the hydrographic observations (c.f., Fig. 16a, c). However, these insights are preliminary and do not represent an exhaustive analysis of the available model solutions. In future work, we aim to further explore the links between biases in MLD, biases in Subantarctic Mode Water formation, and biases in the general circulation.

6.3 The spatial scale of air–sea feedback

In Sect. 3.4 it was shown that the magnitude of the air–sea feedback in winter is about 40 Wm^{-2} per °C, similar to that found by Large and Yeager (2012). In addition, the air–sea heat flux feedback to SST has a spatial scale which is dependent on the wind velocity along the SST gradient, and initial air–sea temperature and humidity difference. Nonaka et al (2009) provided a simple model to predict the restoring time scale of surface air temperature in the Southern Ocean, of around 20 h. Noting that strongest heat fluxes occurred during southerly winds in synoptic storms crossing the quasi-zonal SST fronts, and using a typical wind velocity of 10 m/s in these storms, gives a meridional scale of around 700 km, reasonably consistent with the spatial scale of between 5° and 10° of enhanced air–sea heat loss in observations and POP-HR (Fig. 12a, c). In POP-HR this is an important factor setting the meridional scale of the DMB (Fig. 12c), whereas in POP-RC it acts in combination with salinity advection to give the DMB spatial scale (see Figs. 13, 14).

6.4 Extension to fully coupled models and other ocean-forcing datasets

The results in this paper are specific to ocean-ice simulations forced by the CORE dataset (Large and Yeager 2004, 2009). An obvious question is whether the results would apply to fully coupled models, or to ocean-ice simulations forced by other datasets. Addressing this in full is beyond the scope of the current paper, but investigation by the current authors of the fully coupled versions of CESM1 and CESM2, and of ocean-ice simulations forced by the JRA55-do dataset (Tsujino et al. 2018) revealed qualitatively similar behavior, but quantitative differences were apparent. Specifically any coupled or forced ocean-ice simulations with the low resolution ocean model exhibited the large shallow bias in MLD seen

Fig. 16 Potential vorticity sections at 90° E for February, from **a** POP-HR, **b** POP-LR and **c** WOCE observations. Overlaid contours are potential density (kg m^{-3})
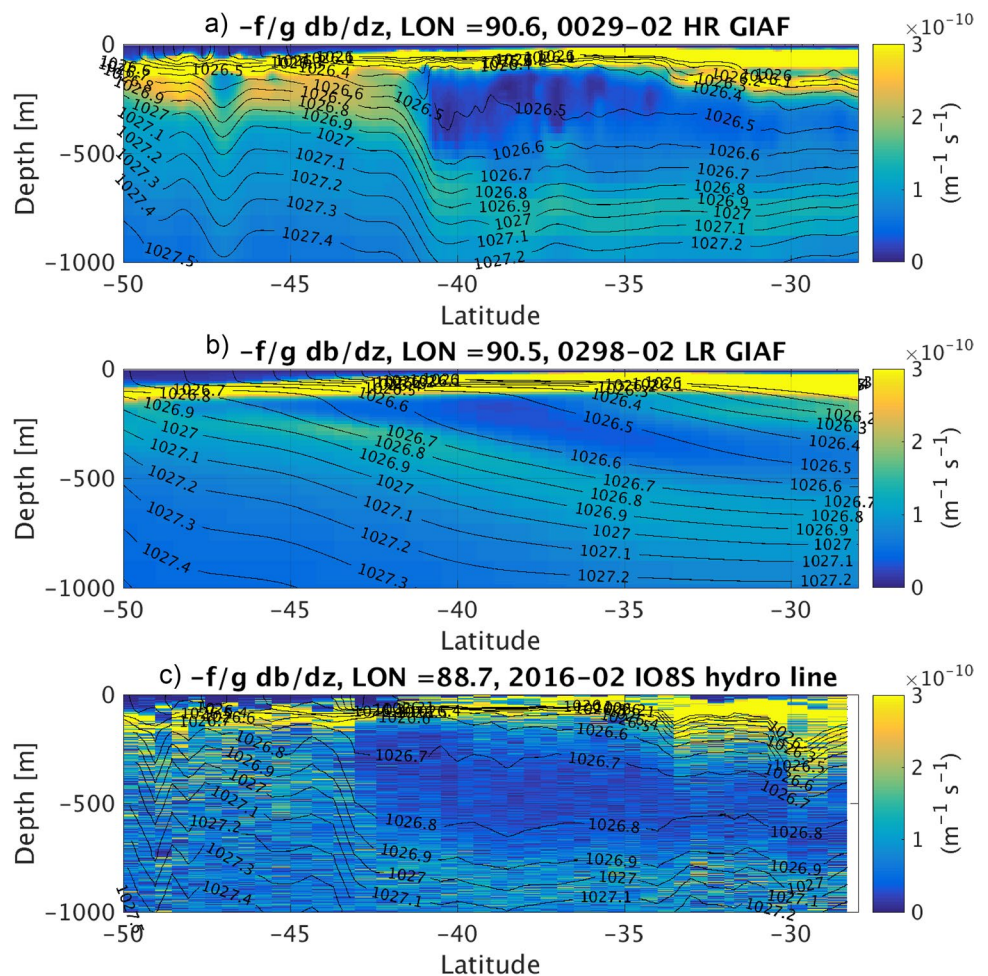
here (see also Sallée et al. 2013; Meijers 2014 for other coupled models), whilst those runs using the 0.1° ocean model had much deeper MLD than with low resolution, sometimes with an over-deep bias in MLD in the S. E. Pacific relative to Argo (see also Gutjahr et al. 2019 who investigated coupled models with 0.4° or 0.1° ocean models). These findings are consistent with the fact that the improved ocean circulation at high-resolution is the key factor, whilst the quantitative differences indicate that other factors, such as strength of the wind, structure of the air–sea heat flux field, etc. also play a role, as these will differ between forced and coupled runs, or forced runs with different forcing dataset.

7 Conclusions

In this paper, a series of global ocean/sea-ice model experiments has yielded new insights into the effects of the climatological geostrophic ocean circulation on the stratification between 200–400 m in the Subantarctic Southern Ocean. Here, the stratification remains weak year-round facilitating a band of deep MLDs, mode water formation, and heat and

greenhouse gas uptake during winter (the deep mixing band, DMB). Changes in the circulation can weaken the stratification in two ways: (1) enhanced southward and/or eastward flow of warm water strengthens surface heat losses (a feedback of about 40 Wm^{-2} C^{-1}) thereby encouraging convection, and (2) enhanced southward and/or eastward flow of salinity at the surface relative to depth increases the density of surface waters relative to those at depth. This work provides the first circumglobal assessment of the contribution of both of these processes to the DMB.

We confirm and extend prior studies by showing that the wintertime MLDs in the DMB exhibit a strong sensitivity to the horizontal grid resolution (up to 100–200 m, depending on MLD definition; comparable to observed ~ 300 to 500 m winter MLDs). A model configuration with a finer eddy-resolving grid and hence improved upper-ocean heat and salinity transport yields a warmer (~ 1 °C), narrower, deeper and thus more realistic DMB than low resolution. In addition, we show for the first time that a simulation with the standard 1° model grid but a geostrophic current that matches observations (via the semi-prognostic method) also yields order-one (~ 100 m) increases in the MLD and

Fig. 17 Annual mean net surface heat flux, with positive values denoting ocean heat loss. All panels share same color bar. Values are an average over 5 years or more as available. **a** Large and Yeager (2009) CORE Interannual forcing and Had-ISST, **b** Trenberth and Fasullo 2017, **c** OAFLUX 0.25 °, **d** J-OFURO3
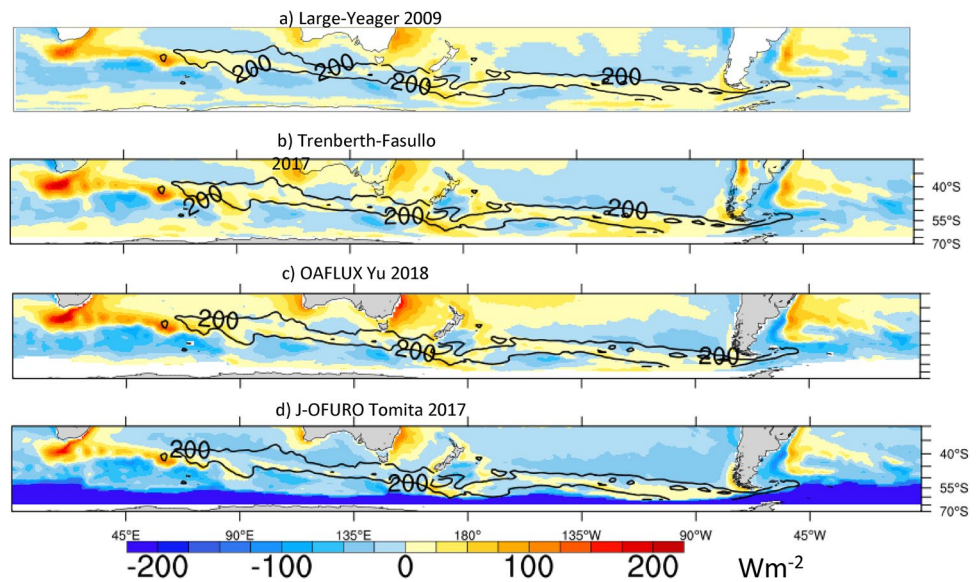
a warmer (~ 1 °C), saltier (~ 0.25 psu) and again more realistic DMB. Although these results are qualitatively similar in both experiments, the warmer SSTs and enhanced air–sea heat loss (increase of 40–80 Wm^{-2}, compared to the observed winter mean 60–120 Wm^2) are a stronger driver of reduced density stratification and hence the deeper DMB in the experiment with a finer grid, whereas the increased upper-ocean salinity is more important in the experiment with the observed circulation. Unsurprisingly, neither grid refinement nor fixing the geostrophic flow fully eliminates the biases in the DMB or provides a uniformly superior simulation, pointing to the need for continued research into other processes affecting the DMB.

Additional 1° experiments with regional application of the semi-prognostic method, and analysis of the transient evolution from the initial condition show that fixing the geostrophic circulation yields improved stratification via both remote and local effects. Warm and salty upper ocean water masses originate in key regions (e.g. the Agulhas Retroflection, as in Wang et al. 2014) and their remote impacts on stratification are felt downstream in the Southern Ocean following the ACC; simultaneously, the local redistribution of heat and salinity pathways within the Southern Ocean leads to convergences of heat and salinity that also modify the stratification in important ways. We find that it takes about 5 years for the improvements arising from the fixed geostrophic ocean current to fully develop, consistent with the advection timescale of the flow in the Subantarctic zone from the south-west Indian Ocean eastwards to Drake Passage.

To put these results in context, we compare the magnitude of the MLD biases that we attribute to biases in the geostrophic flow (~ 100 m) to other plausible biases due to unresolved small-scale processes. Existing crude estimates suggest that Langmuir turbulence (~ 10–60 m; Li and Fox-Kemper 2017; Li et al. 2019), high-frequency winds and near-inertial oscillations (< 100 m; e.g., Jochum et al. 2013; Whitt et al. 2019), and submesoscale ocean processes (~ 100 m; Fox-Kemper et al. 2011) are no larger than the biases due to the geostrophic flow.

Optimistically, the results of the experiments with fixed geostrophic flow suggest that it may be technically feasible to substantially improve the simulation of the DMB without refining the ocean model grid resolution if the appropriate modifications to the numerical schemes and governing equations/parameterizations are applied. However, the results also suggest that parameterization efforts may not be sufficient or even be necessary to improve the simulation of the DMB if they do not also substantially reduce the biases in the resolved geostrophic circulation. In any case, one clear path to an improved simulation of the DMB in a global ocean model involves at least regionally if not globally finer (but not necessarily eddy-resolving, see Lee et al. 2011) grid resolution. Further the results of this paper hint that the finer resolution may be more important for improving the representation of the large-scale climatological currents (ARC, ACC) and associated thermohaline transport that is (imperfectly) resolved on a 1° grid than explicitly representing or improving flows that are unresolved in the standard-resolution model.

Finally, these results raise new questions by exposing the strong sensitivity of the DMB to existing biases in the climatological geostrophic circulation of a CMIP-class ocean model. The results highlight a need for future work to both elucidate the fundamental mechanisms by which the geostrophic circulation impacts the DMB and associated mode water formation and air–sea exchange as well as efforts to
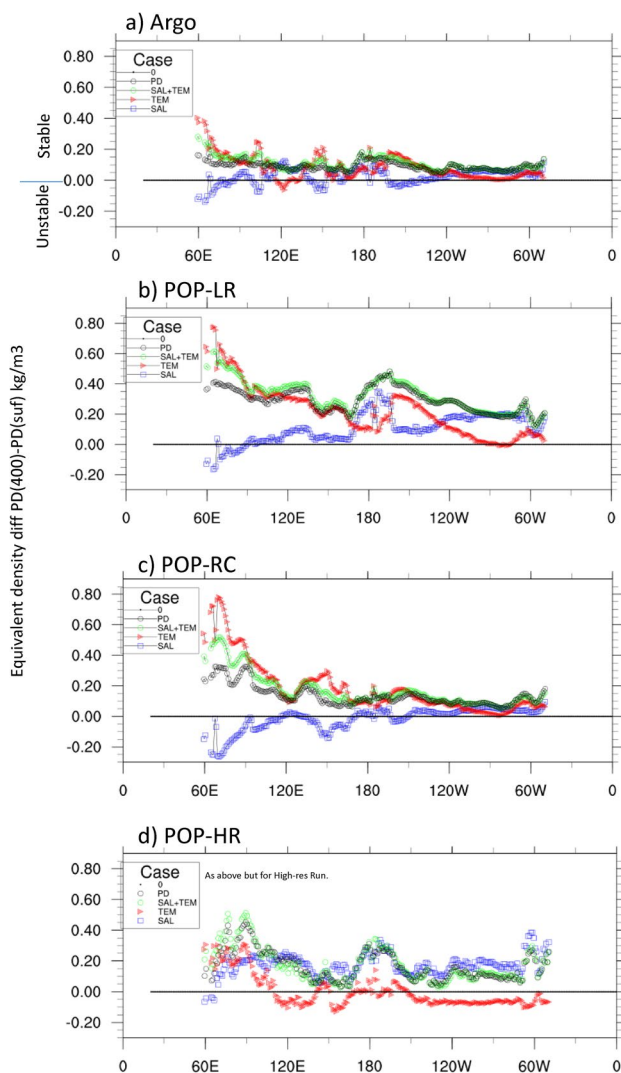
Fig. 18 Temperature and salinity stratification density-equivalent plots. Lines with symbols show the equivalent density stratification PD(400 M)-PD(0 m) obtained using the local EOS for the temperature part (TEM), the salinity part (SAL), and their combination (see legend). Also shown is the density stratification (labelled PD). All are averaged over the latitudes where MLD(ARGO) > 200 m and all results are for Austral winter. **a** Argo, **b** POP-LR, **c** POP-RC, **d** POP-HR. The sign convention for stability is shown on ordinate of **a**

improve the representation of the geostrophic circulation in global ocean and climate models.

Appendix A. Comparison of different air–sea heat flux datasets

Three alternative air–sea heat flux analyses are compared here against the Trenberth and Fasullo (2017) data used in this paper, and against the model simulation results.

CORE (Large and Yeager 2009) is a dataset of atmosphere forcing variables from the National Centers for Environmental Prediction-NCAR (NCEP-NCAR) reanalysis and other datasets that are modified to best fit independent observations. Here we refer to the net air–sea heat flux that is derived by combining HadISST (Hurrell et al. 2008) with the CORE atmosphere forcing datasets, utilizing the bulk flux algorithm of Large and Yeager (2004, 2009). Long-term averages of the CORE inter-annually varying dataset are used.

The Objectively Analyzed Air–sea Fluxes (OAFLUX) product (Yu and Weller 2007) uses variational objective analysis to combine satellite retrievals of wind and humidity and SST with reanalysis data of the same variables and also air temperature. The COARE 3.0 bulk flux algorithm (Fairall et al. 2003) was used to compute bulk fluxes. The original product is available at 1° for Global ice-free oceans and extends from 1958 to near present, with the period prior to the 1980s being governed by reanalysis-only data. We use a preliminary new 0.25° dataset, based solely on satellite data, provided by Lisan Yu (pers. comm. 2018).

The Japanese Ocean Flux data sets with use of Remote Sensing Observations version 3 (JOFURO-3) is the evolution of the original J-OFURO dataset (Kubota et al. 2002).

The new version is available for 1996–2013, daily mean at 0.25°. The dataset is derived solely from satellite-data product except for 2 m air temperature taken from NCEP-DOE reanalysis. The fluxes are derived using the COARE3.0 bulk flux algorithm (Fairall et al. 2003). Full details of the dataset are given in Tomita et al. (2018).

Figure 17 shows the long term annual average net surface heat loss in the Southern Ocean from various observed products. The CORE and Trenberth and Fasullo (2017) products are quite similar, while J-OFUROv3 has a fairly clear bias towards heat gain (negative values in Fig. 17), and OAF-LUX 0.25° has overall more heat loss. For our purposes, the important question is whether differences between model and observations are qualitatively similar between observed products. To this end Supp. Fig. S17 shows the difference between POP-LR and the various products for the annual mean net surface heat loss. In all cases the bias of low surface heat loss in the DMB and to its west in the Indian Ocean is quite clear. In the East Pacific Ocean however, there are some notable differences between results based on different products, and e.g. the bias is weakly positive compared to J-OFURO and OAFLUX but negative compared to Trenberth and Fasullo (2017). We conclude that the low surface heat loss bias in POP-LR is robust from the Indian Ocean to west Pacific Ocean, but is uncertain in the east Pacific.

Appendix B. Quantification of role of temperature vs salinity in setting stratification differences

A local Equation of State (EOS) is applied to help explain the results of Sect. 3.4 on upper ocean stratification differences between models and observations. The EOS is written as

$$\rho = \sigma_0 + \rho_{ref}\{\beta(S - S_{ref}) - \alpha(T - T_{ref})\}.$$

Here ρ is potential density, σ_0 and ρ_{ref} are reference densities, α and β are expansion coefficients for temperature and salinity, defined by

$$\alpha = -\frac{1}{\rho}\frac{\partial\rho}{\partial T} \text{ and } \beta = \frac{1}{\rho}\frac{\partial\rho}{\partial S},$$

α and β are dependent on the local temperature and salinity as described by McDougall et al. (2003). A reference state of $T_{ref} = 5$ °C and $S_{ref} = 34$psu is used, which is a representative Southern Ocean value. The reference density is the density at those same reference values of temperature and salinity.

Next the individual contributions of temperature and salinity to the density stratification are used, i.e.:

$$\{\rho(400) - \rho(0)\}|_T = -\rho_{ref}\{\alpha_{400}T(400) - \alpha_0 T(0)\},$$

$$\{\rho(400) - \rho(0)\}_S| = \rho_{ref}\{\beta_{400}S(400) - \beta_0 S(0)\},$$

are the temperature and salinity contributions respectively. Here α and β depend on the model (or observed as appropriate) T, S, and pressure p, so that e.g. $\alpha_0 = \alpha(T,S,p(5\text{ m}))$ and $\alpha_{400} = \alpha(T,S,p(5\text{ m}))$. (Note that we aim to estimate potential density so that 5 m (nearest cell to surface) is used instead of 400 m in the latter.)

The linear contributions to the potential density stratification are shown in Fig. 18 together with the actual potential density stratification, the latter to test the accuracy of the linear fit. Note that using the above reference state gives a very good fit to the total density east of 120° E, as shown by comparing the sum of the linear temperature and salinity contribution in Fig. 18 (green line) with the actual potential density stratification (black line). However, west of 120° E the estimate using the linear EOS gives more stable values than the actual potential density (Fig. 18). This is because the DMB is in significantly warmer and saltier water than the reference state in the south–west Indian Ocean part of the DMB, due to the influence of the Agulhas return Current. If we used instead a warmer and saltier reference state of say $T_{ref} = 15$ °C and $S_{ref} = 35$psu, the fit to actual potential density is near-perfect west of 90 W but heavily degraded further east, whilst using in between values of $T_{ref} = 7.5$ °C and $S_{ref} = 34.4$psu gives improved fit west of 120 E but again is degraded further east in the Pacific Ocean (results not shown). We choose the reference state of $T_{ref} = 5$ °C and $S_{ref} = 34$psu because it gives a good fit in the Pacific Ocean where there are subtle differences in density stratification due to temperature vs salinity (T vs S) which we want to resolve and understand, whereas in the south-west Indian Ocean the relative contributions of T&S are more clearly defined and qualitatively not sensitive to error in the linear fit.

Starting with the observations from Argo, it can be seen that the density stratification is governed mostly by temperature in the west Indian Ocean and in most of the DMB as far east as 120° W (Fig. 18a). East of 120° W temperature plays a minor role and the stratification is due to salinity.

In POP-LR, density stratification is too strong in the Indian Ocean compared to Argo due mainly to temperature (Fig. 18b). Salinity then dominates the density stratification from 170° E to 170° W, and then temperature from 170° W to 130° W: both make the density stratification too strong compared to observations. East of 130° W salinity dominates the over-strong density stratification.

For POP-RC, the situation is very different in the eastern hemisphere than in the western hemisphere. In the Indian

Ocean, overall density stratification is reduced compared to POP-LR, but the thermal stratification is too strong compared to observations (Fig. 18c), and it is compensated by too-unstable salinity stratification. By contrast, east of 180° W the density stratification in POP-RC well matches the Argo observations described above.

Finally, for POP-HR, as expected from Sect. 3, the thermal stratification is much weakened compared to POP-LR and becomes too unstable compared to obs: this is overcompensated by too stable salinity stratification so that the density stratification averaged over the DMB is too strong compared to observations (Fig. 18d). (But at some specific locations within the DMB the stratification may be weaker than observed and MLD may exceed observations, as seen in Fig. 1).

References

Argo (2019) Argo float data and metadata from Global Data Assembly Centre (Argo GDAC). SEANOE. https://doi.org/10.17882/42182

Bachman SD et al (2017) Parameterization of frontal symmetric instabilities. I: theory for resolved fronts. Ocean Model 109:72–95

Bachman SD (2019) The GM+E closure: a framework for coupling backscatter with the Gent and McWilliams parameterization. Ocean Model 136:85–106

Brankart JM (2013) Impact of uncertainties in the horizontal density gradient upon low resolution global ocean modelling. Ocean Model 66:64–76

Cerovečki I, Meijers AJS, Mazloff MR, Gille ST, Tamsitt VM, Holland PR (2019) The effects of enhanced sea ice export from the Ross Sea on recent cooling and freshening of the Southeast Pacific. J Clim 32:2013–2035

Cerovečki I, Talley LD, Mazloff MR, Maze G (2013) Subantarctic mode water formation, destruction and export in the eddy-permitting Southern Ocean state estimate. J Phys Oceanogr 43:1485–1511

de Boyer Montégut C, Madec G, Fischer AS, Lazar A, Iudicone D (2004) Mixed layer depth over the global ocean: an examination of profile data and a profile-based climatology. J Geophys Res 109:C12003. https://doi.org/10.1029/2004JC002378

Danabasoglu G, Mc Williams JC (1995) Sensitivity of the global ocean circulation to parameterizations of mesoscale tracer transports. J Clim 8(12):2967–2987

Danabasoglu G, Large WG, Tribbia JJ, Gent PR, Briegleb BP, McWilliams JC (2006) Diurnal coupling in the tropical oceans of CCSM3. J Clim 19(11):2347–2365

Danabasoglu G, Bates SC, Briegleb BP, Jayne SR, Jochum M, Large WG, Peacock S, Yeager SG (2012) The CCSM4 ocean component. J Clim 25:1361–2138

Deardorff JW, Willis GE, Lilly DK (1969) Laboratory investigation of non-steady penetrative convection. J Fluid Mech 35:7–31

Doney SC et al (2004) Evaluating global ocean carbon models: the importance of realistic physics. Global Biogeochem Cycles 18:GB3017. https://doi.org/10.1029/2003GB002150

Dong S, Sprintall J, Gille ST, Talley L (2008) Southern Ocean mixed layer depth from Argo float profiles. J Geophys Res 113:C06013. https://doi.org/10.1029/2006JC004051

Drews A, Greatbatch RJ (2017) Evolution of the Atlantic multidecadal variability in a model with an improved North Atlantic Current. J Clim 30:5491–5512

DuVivier AK, Large WG, Small RJ (2018) Argo observations of the deep mixing band in the Southern Ocean: a salinity modeling challenge. J Geophys Res Oceans. https://doi.org/10.1029/2018JC014275

Fairall CW, Bradley EF, Hare JE, Grachev AA, Edson JB (2003) Bulk parameterization of air-sea fluxes: Updates and verification for the COARE algorithm. J Clim 16:571–591

Forryan A et al (2015) Rapid injection of near-inertial shear into the stratified upper ocean at an Antarctic Circumpolar Current front. Geophys Res Letts 42:3431–3441

Fox-Kemper B, Danabasoglu G, Ferrari R, Griffies SM, Hallberg RW, Holland MM, Maltrud ME, Peacock S, Samuels BL (2011) Parameterization of mixed layer eddies. III: implementation and impact in global ocean climate simulations. Ocean Model 39:61–78

Frölicher TL, Sarmiento JL, Paynter DJ, Dunne JP, Krasting JP, Winton M (2015) Dominance of the Southern Ocean in Anthropogenic Carbon and heat uptake in CMIP5 models. J Clim 28:862–886

Gao L, Rintoul SR, Yu W (2018) Recent wind-driven changes in Subantarctic Mode Water and its impact on ocean heat storage. Nat Clim Change 8:58–63

Gent PR (2011) The Gent-McWilliams parameterization: 20/20 hindsight. Ocean Mod 39:2–9

Gent PR, McWilliams JC (1990) Isopycnal mixing in ocean circulation models. J Phys Oceanogr 20:150–155

Greatbatch RJ, Sheng J, Eden C, Tang L, Zhai X, Zhao J (2004) The semi-prognostic method. Cont Shelf Res 24:2149–2165

Gutjahr O, Putrasahan D, Lohmann K, Jungclaus JH, von Storch J-S, Bruggemann N, Haak H, Stossel A (2019) Max Planck Institute Earth System Model (MPI-ESM12) for the High-Resolution Model Intercomparison Project (HighResMIP). Geosci Model Dev. https://doi.org/10.5194/gmd-12-3241-2019

Hanawa K, Talley LD (2001) Mode waters, 373–386. In: Seidler G, Church J, Gould J (eds) Ocean circulation and climate. Academic Press, Cambridge, p 715

Hausmann U, Czja A, Marshall J (2016) Estimates of air-sea feedbacks on sea surface temperature anomalies in the Southern Ocean. J Clim 29:439–454

Herraiz-Borreguero L, Rintoul SR (2011) Subantarctic mode water: distribution and circulation. Ocean Dyn 61:103–126. https://doi.org/10.1007/s10236-010-0352-9

Heuzé C, Vivier F, Le Sommer J, Molines J-M, Penduff T (2015) Can we map the interannual variability of the whole upper Southern Ocean with the current database of hydrographic observations. J Geophys Res 120:7960–7978. https://doi.org/10.1002/2015JC011115

Holte J, Talley LD, Gilson J, Roemmich D (2017) An Argo mixed layer climatology and database. Geophys Res Lett 44:5618–5626. https://doi.org/10.1002/2017GL073426

Hunke EC, Lipscomb WH (2008) CICE: the Los Alamos sea ice model user's manual, version 4. Los Alamos National Laboratory Tech. Rep. LA-CC-06–012

Hurrell JW et al (2013) The community earth system model: a framework for collaborative research. Bull Am Meteorol Soc 94:1339–1360

Hurrell JW, Hack JJ, Shea D, Caron JM, Rosinski J (2008) A new sea surface temperature and sea ice boundary dataset for the community atmosphere model. J Clim 21:5145–5153

Hyder P et al (2018) Critical Southern Ocean climate model biases traced to atmospheric model cloud errors. Nat Commun 9:3625. https://doi.org/10.1038/s41467-018-05634-2

Jochum M et al (2013) The impact of oceanic near-inertial waves on climate. J Clim 26:2833–2844

Johnson BK, Bryan FO, Grodsky SA, Carton JA (2016) Climatological annual cycle of the salinity budgets of the Subtropical Maxima. J Phys Oceanogr 46:2981–2994

Kubota M, Iwasaka N, Kizu S, Konda M, Kutsuwada K (2002) Japanese Ocean Flux data sets with use of remote sensing observations (J-OFURO). J Oceanogr 58:213–225

Large WG, Danabasoglu G, Doney SC, McWilliams JC (1997) Sensitivity to surface forcing and boundary layer mixing in a global ocean model: annual-mean climatology. J Phys Oceanogr 27:2418–2447

Large WG, McWilliams JC, Doney SC (1994) Oceanic vertical mixing: a review and a model with nonlocal boundary layer parameterization. Rev Geophys 32:363–403

Large WG, Yeager SG (2004) Diurnal to decadal global forcing for ocean and sea-ice models: the data sets and flux climatologies. NCAR Technical Note NCAR/TN-460+STR. https://opensky.ucar.edu/islandora/object/technotes:434. Accessed Mar 2019

Large WG, Yeager SG (2009) The global climatology of an interannually varying air–sea flux data set. Clim Dyn 33:341–364

Large WG, Yeager SG (2012) On the observed trends and changes in global sea surface temperature and air–sea heat fluxes (1984–2006). J Clim 25:6123–6135

Large W, Patton E, DuVivier A, Sullivan P (2019) Similarity theory in the surface layer of large-eddy simulations of the southern ocean with waves. J Phys Oceanogr (**submitted**)

Lee M-M, Nurser AJG, Stevens I, Sallée J-B (2011) Subduction over the Southern Indian Ocean in a high-resolution atmosphere-ocean coupled model. J Clim 24:3830–3849

Levitus S, Boyer T, Conkright M, Johnson D, O'Brien TD, Antonov J, Stephens C, Gelfeld R (1998) Introduction, Vol. 1, World Ocean Database 1998. NOAA Atlas NESDIS 18, 346pp

Li Q, Fox-Kemper B (2017) Assessing the effects of Langmuir turbulence on the entrainment buoyancy flux in the ocean surface boundary layer. J Phys Oceanogr 47:2863–2886

Li Q, Lee S (2017) A mechanism of mixed layer formation in the Indo-Western Pacific Southern Ocean: preconditioning by an eddy-driven jet-scale overturning circulation. J Clim 47:2755–2772

Li Q, Reichl BG, Fox-Kemper B, Adcroft AJ, Belcher SE, Danabasoglu G et al (2019) Comparing ocean surface boundary vertical mixing schemes including Langmuir turbulence. J Adv Model Earth Sys. https://doi.org/10.1029/2019MS001810

Liu C et al (2015) Combining satellite observations and reanalysis energy transports to estimate global net surface energy fluxes 1985–2012. J Geophys Res Atm. https://doi.org/10.1002/2015JD023264

Long MC, Lindsay K, Peacock S, Moore JK, Doney SC (2013) Twentieth-Century Oceanic Carbon Uptake and Storage in CESM1(BGC). J Clim 26:6775–6800. https://doi.org/10.1175/JCLI-D-12-00184.1

Luyten JR, Pedlosky J, Stommel H (1983) The ventilated thermocline. J Phys Oceanogr 13:292–309

McCartney MS (1982) The subtropical recirculation of mode waters. J Mar Res 40:427–464

McClean J et al (2011) A prototype two-decade fully-coupled fine-resolution CCSM simulation. Ocean Model 39:10–30

McDougall TJ, Jackett DR, Wright DR, Feistel R (2003) Accurate and computationally efficient algorithms for potential density and density of seawater. J Atmos Ocean Tech 20:730–741

McWilliams JC, Huckle E, Liang J, Sullivan PP (2014) Langmuir turbulence in swell. J Phys Oceanogr 44:870–890

McWilliams JC, Sullivan PP, Moeng C-H (1997) Langmuir turbulence in the ocean. J Fluid Mech 334:1–30

Meijers AJS (2014) The Southern Ocean in the Coupled Model Intercomparison project. Phil Trans Roy Soc A 372:20130296

Nonaka M, Nakamura H, Taguchi B, Komori N, Kuwano-Yoshida A, Takaya K (2009) Air–sea heat exchanges characteristic of a prominent midlatitude ocean front in the Southern Indian Ocean as simulated in a high-resolution coupled CGM. J Clim 22:6515–6535

Pollard RT, Rhines PB, Thompson RORY (1972) The deepening of the wind-mixed layer. Geophys Fluid Mech 4:381–404

Redi MH (1982) Oceanic isopycnal mixing by coordinate rotation. J Phys Oceanogr 12:1154–1158

Reichl BG, Wang D, Hara T, Ginis I, Kukulka T (2016) Langmuir turbulence parameterization in Tropical Cyclone conditions. J Phys Oceanogr 46:863–886

Rhines PB (1986) Vorticity dynamics of the oceanic general circulation. Ann Rev Fluid Mech 18:433–497

Ringler T, Petersen M, Higdon RL, Jacobsen D, Jones PW, Maltrud M (2013) A multi-resolution approach to global ocean modeling. Ocean Model 69:211–232

Risien CM, Chelton DB (2008) A global climatology of surface wind and wind stress fields from eight years of QuikSCAT scatterometer data. J Phys Oceanogr 38:2379–2413

Rodgers KB et al (2014) Strong sensitivity of Southern Ocean carbon uptake and nutrient cycling to wind stirring. Biogeosciences 11:4077–4098

Roemmich D, Gilson J (2009) The 2004–2008 mean and annual cycle of temperature, salinity and steric height in the global ocean from the Argo program. Prog Oceanogr 82:81–100

Roemmich D, Johnson G, Riser S, Davis R, Gilson J, Owens W, Garzoli S, Schmid C, Ignaszewski M (2009) The Argo program: observing the global ocean with profiling floats. Oceanography 22:23–43

Sabine CL et al (2004) The Oceanic sink for Anthropogenic CO_2. Science 305:367–371

Sallée J-B, Shuckburgh E, Bruneau N, Meijers AJS, Barcegirdle TJ, Wang Z (2013) Assessment of Southern Ocean mixed-layer depths in CMIP5 models: historical bias and forcing response. J Geophys Res 118:1845–1862. https://doi.org/10.1002/jgrc.20157

Sheng J, Greatbatch RJ, Wright DG (2001) Improving the utility of ocean circulation models through adjustment of the momentum balance. J Geophys Res 106:16711–16728

Smith RD, et al (2010) The Parallel Ocean Program (POP) reference manual. Los Alamos National Laboratory Tech. Rep. LAUR-10–01853

Stanley Z, Grooms I, Kleiber W, Bachman SD, Castruccio F, Adcroft A (2020) Parameterizing the impact of unresolved temperature variability on the large-scale density field part I: Theory. Submitted to J Adv Model Earth Sys

Tamsitt V, Talley LD, Mazloff MR, Cerovecki I (2016) Zonal variations in the Southern Ocean heat budget. J Clim 29:6563–6579

Thomas LN (2005) Destruction of potential vorticity by winds. J Phys Oceanogr 35:2457–2466

Thompson AF, Sallée J-B (2011) Jets and topography: jet transitions and the impact on transport in the Antarctic Circumpolar Current. J Phys Oceanogr 42:956–972

Tomita H, Hihara T, Kato S, Kubota M, Kutsuwada K (2018) An introduction to J-OFURO3, a third-generation Japanese ocean flux data set using remote-sensing observations. J Oceanogr. https://doi.org/10.1007/s10872-018-0493-x

Trenberth KE, Fasullo JT (2017) Atlantic meridional heat transports computed from balancing Earth's energy locally. Geophys Res Lett. https://doi.org/10.1002/2016GL071833

Tsujino H, Urakawa S, Nakano H, Justin Small R, Kim WH, Yeager SG, Danabasoglu G, Suzuki T, Bamber JL, Bentsen M, Böning CW, Bozec A, Chassignet EP, Curchitser E, Dias FB, Durack PJ, Griffies SM, Harada Y, Ilicak M, Josey SA, Kobayashi C, Kobayashi S, Komuro Y, Large WG, Le Sommer J, Marsland SJ, Masina S, Scheinert M, Tomita H, Valdivieso M, Yamazaki D (2018) JRA-55 based surface dataset for driving ocean–sea-ice models (JRA55-do). Ocean Model 130:79–139

Vallis GK (2000) Large-scale circulation and production of stratification: effects of wind, geometry, and diffusion. J Phys Oceanogr 30:933–954

Wang J, Mazloff MR, Gille ST (2014) Pathways of the Agulhas waters poleward of 29° S. J Geophys Res Oceans. https://doi.org/10.1002/2014JC010049

Weese SR, Bryan FO (2006) Climate impacts of systematic errors in the simulation of the path of the North Atlantic Current. Geophys Res Letts. https://doi.org/10.1029/2006GL027669

Weijer W et al (2012) The Southern Ocean and its climate in CCSM4. J Clim 25:2652–2675

Whitt DB, Taylor JR (2017) Energetic submesoscales maintain strong mixed layer stratification during an autumn storm. J Phys Oceanogr 47:2419–2427

Whitt D, Nicholson SA, Carranza MM (2019) Global impacts of subseasonal (< 60 day) wind variability on ocean surface stress, buoyancy flux, and mixed layer depth. J Geophys Res accepted

Wijeratne S, Pattiaratchi C, Procter R (2018) Estimates of surface and subsurface boundary current transport around Australia. J Geophys Res. https://doi.org/10.1002/2017JC013221

Yu L, Weller RA (2007) Objectively analyzed air–sea heat fluxes for the global ice-free oceans (1981–2005). Bull Am Meteorol Soc 88:527–539